Title

A self-limiting mechanotransduction feedback loop ensures robust organ formation

Authors

Yusuke Mori[1,2], Paul Robin[3], Anne Belle Briggs[1], Daniel S. Levic[1], Jiacheng Wang[1], Kira L. Heikes[1], Michel Bagnat[1], Edouard Hannezo[3], Akankshi Munjal[1,4]

[1] Department of Cell Biology, Duke University School of Medicine, Durham, NC 27710, USA

[2] Duke Regeneration Center, Duke University School of Medicine, Durham, NC 27710, USA

[3] Institute of Science and Technology, Am Campus 1, 3400 Klosterneuburg, Austria

[4] Correspondence: akankshi.munjal@duke.edu

Abstract

Organ morphogenesis uses mechanotransduction feedback loops to convert forces into gene expression changes that regulate cell mechanics. How these loops integrate with developmental programs to ensure robust outcomes remains unclear. We show Yap mechanotransduction establishes a self-limiting positive feedback loop for semicircular canal formation in zebrafish. Canal development proceeds through bud initiation, extension, and fusion within the otic epithelium. Local swelling of hyaluronan-rich extracellular matrix (ECM) in the bud activates Yap in a spatial pattern. Yap induces its target *ccn1l1*, promoting further ECM expansion to sustain bud extension. This feedback loop confers developmental robustness: graded knockdown of *ccn1l1* reduces extension rate, yet canal formation persists and fails only with strong disruption. Critically, the loop contains its own termination mechanism. During bud fusion, PKA-CREB signaling, activated by an adhesion GPCR, *gpr126,* suppresses *ccn1l1*, ending the loop. These findings reveal how mechanotransduction loops with built-in termination provide developmental control by integrating mechanical forces, transcriptional responses, and morphogenetic outcomes.

Main

Signaling pathways employ sophisticated feedback mechanisms to control tissue morphogenesis – the process by which tissues remodel into complex and functional

organs[1,2]. Such feedback interactions can take the form of temporal switches or self-limiting circuits, for example, the morphogen Nodal induces its own inhibitor, Lefty, to establish early embryonic patterning[3,4]. Beyond biochemical signals, developing tissues also experience and respond to physical forces. Mechanotransduction pathways sense forces such as compression, stretching, or shear, and convert them into transcriptional responses that remodel the physical environment, creating feedback loops between mechanics and gene expression during morphogenesis[5,6].

Yes-associated protein 1 (Yap), a transcriptional co-activator of the Hippo pathway, is a central mechanotransducer[7]. In response to force, Yap and its co-activator Taz translocate to the nucleus, where they bind to the transcription factor Tead to activate genes that regulate proliferation, differentiation, and extracellular matrix (ECM) production[7]. By linking mechanical inputs to transcriptional programs that reshape tissue architecture, Yap provides a molecular basis for feedback between mechanics and gene expression[8,9]. Yet how such mechanotransduction feedback loops are spatially and temporally organized during development and how they are ultimately terminated to avoid unchecked amplification or premature growth restriction remains poorly understood. Understanding these principles is central to explaining how complex organ shapes emerge from the interplay of signals, forces, and transcriptional programs.

The zebrafish semicircular canals (SCCs) enable addressing these questions because they allow for the simultaneous measurement of transcriptional, biochemical, and mechanical dynamics during morphogenesis[10]. SCCs arise from the otic vesicle (OV) epithelium through three discrete steps: initiation of bud formation at six zones, extension of these buds, and the fusion of adjacent bud pairs that results in the formation of three pillar-shaped structures that delineate the three SCCs. Bud initiation is driven by localized synthesis of a hyaluronan (HA)– and Versican–rich ECM that osmotically swells, pushing the overlying cells[10,11]. How this process, initiated in a small group of cells, achieves the systems-level coordination necessary to ensure the buds extend to the right size and fuse successfully remains unknown. We hypothesized that mechanotransduction could provide this coordinating mechanism by linking the local ECM expansion to transcriptional responses and morphogenetic outcomes.

Our work reveals that SCC morphogenesis is driven by a self-limiting positive feedback loop operating through Yap mechanotransduction. Using a combination of quantitative imaging, theoretical modeling, and a live knock-in reporter of endogenous Yap, we observe that ECM expansion mechanically activates Yap in a spatially patterned manner, with peak activity at the bud border, recruiting these cells into the growing bud. Yap in turn induces *cellular communication network factor 1-like 1* (*ccn1l1,* also known as *cyr61l1*), a matricellular protein that promotes HA and Versican synthesis, ensuing rapid ECM expansion. Progressive loss of the Yap-Ccn1l1-ECM loop led to a dose-dependent reduction in bud extension rates, yet fusion remained robust at lower levels of disruption and was abolished only at the highest dose.

Termination of this loop occurs during bud fusion when *ccn1l1* expression declines. Analysis of mutants in a conserved adhesion GPCR, *gpr126*, previously shown to block bud fusion, revealed that *ccn1l1* expression persists, resulting in uncontrolled growth. Mechanistically, the activation of Gpr126 signaling during bud fusion results in phosphorylation and activation of the transcription factor CREB, which suppresses *ccn1l1* expression. Thus, the morphological outcome of positive feedback–bud fusion–serves as a stop signal that terminates the very process it drives–bud extension.

Results

ECM swelling-mediated Yap activation is required for bud extension

The SCC in zebrafish develops through the remodeling of the lumenized single-layered embryonic inner ear epithelium, the basement membrane (BM)-enclosed OV, at six "canal-genesis zones" (Fig. 1a)[10,12]. Morphogenesis begins at 45 hours post fertilization (hpf) with the initiation of buds at antero-lateral, postero-lateral, and anterior zones, where cells extend into the lumen with reduced BM contact[10,13]. By 50 hpf, these buds extend, and a posterior bud begins to form. By 60 hpf, antero-lateral and anterior buds fuse, while postero-lateral and posterior buds extend, and ventral and ventro-lateral budding begins. By 72 hpf, all bud pairs fuse to form the anterior, posterior, and ventral pillars, which demarcate the three semicircular canals. We focused our analysis on the anterior buds,

90 which provide a clear example of all morphogenetic steps: pre−budding (40 hpf), initiation
91 (45-48 hpf), extension (48-55 hpf), and fusion (55 hpf).

92 We recently demonstrated that the transcription factor Lmx1b promotes the expression
93 of *hyaluronan synthase 3 (has3)* and *versican b (vcanb),* which encode enzymes for HA
94 and Versican synthesis, respectively, at canal-genesis zones[11]. Charged HA polymers
95 and the proteoglycan Versican that binds HA are secreted basally into the ECM, and
96 osmotic swelling of this HA-rich ECM generates pressure that pushes the overlying
97 epithelium into buds[11]. Longitudinal bud extension is maintained by tangentially
98 distributed actomyosin tethers, known as cytocinches[10]. Because ECM swelling imposes
99 mechanical stress on budding cells[10] (Extended Fig. 1a-c), we asked whether this stress
100 engages the Yap mechanotransduction pathway.

101 To characterize the dynamic localization of endogenous Yap protein *in vivo*, we
102 established a *TgKI(Yap1-mScarlet)* reporter line using a knock-in tagging method[14] (Fig.
103 1b-b'). Yap activity was quantified by calculating the nuclear-cytoplasmic ratio in budding
104 cells in embryos co-injected with H2B-EGFP mRNA to visualize the nuclei. Prior to
105 budding (40 hpf), Yap was inactive, with a nuclear-to-cytoplasmic ratio around 1. During
106 anterior bud extension at 50 hpf, the ratio increased above 1, indicating active Yap (Fig
107 1c). We also observed a few cells in the dorsal non-budding region of the OV with a
108 nuclear-to-cytoplasmic ratio greater than 1 at various stages of canal morphogenesis (Fig.
109 1b and Extended Fig. 1d).

110 To test whether osmotic swelling of the HA-rich bud-ECM activates Yap in budding cells,
111 we injected hyaluronidase (HAase), an enzyme that degrades HA polymers, into the
112 region surrounding the OV (periotic space). As previously reported, HAase treatment
113 caused shrinkage of the bud-ECM, reduced cell stretching, and inhibited bud
114 extension[10,15] (Extended Fig. 1e-h). Significantly, nuclear localization of Yap was
115 decreased in HAase-treated embryos, with the nuclear-to-cytoplasmic ratio less than 1
116 (Fig. 1d-e). HAase treatment had no effect on the nuclear-to-cytoplasmic ratio of non-
117 budding cells in the dorsal OV (Extended Fig. 1i). These findings were further confirmed
118 by Yap immunostaining experiments, in which the nuclear-to-cytoplasmic ratio in budding

119 cells was greater than 1 in controls but reduced to around 1 in HAase-treated embryos
120 (Extended Fig. 1j-m). Together, these results demonstrate that the osmotic swelling of
121 the bud-ECM induces Yap activation in budding cells.

122 To examine the functional role of Yap, we performed knockdown of *yap1* using a
123 previously characterized morpholino (MO)[16]. Notably, *yap1* knockdown significantly
124 inhibited bud elongation (Fig. 1f-g), resulting in shorter lateral, anterior, and posterior buds
125 at 50 hpf. By 72 hpf, despite the formation of all six buds, 88% of *yap1* morphants failed
126 to initiate pillar formation and consequently did not develop SCCs (Extended Fig. 1n-o).
127 These data demonstrate that Yap is required for successful SCC formation. To uncover
128 the molecular mechanisms underlying this effect, we next examined Yap's downstream
129 transcriptional targets.

130 **Yap-target *ccn1l1* expression is Yap-independent at initiation and Yap-dependent**
131 **during bud extension**

132 To identify downstream targets of Yap, we used available single-cell transcriptomic
133 atlases[17,18]. A zebrafish inner-ear-specific atlas noted expression of a candidate gene,
134 *ccn1l1*, in the SCC-forming cell cluster of the OV, and this expression pattern was
135 validated at the canal-genesis zone during pre-budding and bud extension stages[17,18]. A
136 similar enrichment was observed in the embryo-wide Daniocell atlas[19,20], where
137 annotation of canal-forming cells using *vcanb* (Versican core protein) revealed *ccn1l1*
138 among the top 10 differentially expressed genes (Fig. 2a–b, Extended Fig. 2a). Ccn1l1 is
139 a paralog of Ccn1 and a member of the CCN family of matricellular proteins[21–23], which
140 are known downstream targets of Yap[24–27]. Importantly, the 5' upstream region of *ccn1l1*
141 contains three conserved TEAD-binding motifs recognized by Yap/Taz
142 (GGAATG/CATTCC)[24,28–30] (Extended Fig. 2b).

143 To quantitatively analyze *ccn1l1* expression dynamics at various developmental stages,
144 we used multiplexed hybridization chain reaction (HCR) fluorescence *in situ* hybridization
145 (FISH)[31]. Consistent with the single-cell atlases[32,18], *ccn1l1* expression was restricted to
146 the canal-genesis zones (Fig. 2c-d), and was detectable before bud formation at 40 hpf.

147 Its expression increased significantly during bud extension at 50 hpf, and was
148 subsequently downregulated to background levels upon bud fusion at 60 hpf (Fig. 2e).
149 Importantly, MO-mediated *yap1* knockdown led to a 50% reduction in *ccn1l1* expression
150 during bud extension (Fig. 2f-g), making it comparable to levels at the pre-budding stage,
151 confirming that *ccn1l1* is a Yap target. In contrast, *yap1* knockdown did not affect the
152 onset of *ccn1l1* expression at the pre-budding stage (Extended Fig. 2c-d). These findings
153 demonstrate that Yap is essential for increasing *ccn1l1* expression during bud extension,
154 but not for its initial onset.

155 To understand the initial regulation of *ccn1l1*, we examined its relationship with *lmx1bb*,
156 the transcription factor that, together with its paralog *lmx1ba,* we previously demonstrated
157 patterns HA and Versican synthesis during the pre-budding stage[11]. In the *lmx1bb* null
158 mutants (*lmx1b* $^{jj410/jj410}$)[31], which carry a premature stop codon, we observed a 30.1%
159 reduction of *ccn1l1* expression at the pre-budding zone compared to sibling controls
160 (Extended Fig. 2e-f). Pharmacological inhibition of Notch signaling with RO4929097,
161 which expands *lmx1bb* expression[11], similarly expanded *ccn1l1* expression compared to
162 controls (Extended Fig. 2g).

163 Altogether, these findings reveal a two-stage regulatory mechanism: Lmx1bb in part
164 initiates *ccn1l1* expression during pre-budding, while Yap amplifies *ccn1l1* expression
165 during extension. Given that Yap sustains bud extension, we hypothesized that *ccn1l1*
166 might promote the synthesis of HA and Versican, which drive bud extension. We next
167 investigated the function of *ccn1l1* to test this possibility.

168 **Ccn1l1 promotes HA and Versican synthesis to create a positive feedback loop**

169 To investigate the function of *ccn1l1*, we performed CRISPR-Cas9 or MO-mediated
170 *ccn1l1* knockdown. Consistent with its pre-budding expression pattern, the knockdown of
171 *ccn1l1* blocked the onset of budding, resulting in an absence of buds at 50 hpf and no
172 SCCs at 72 hpf (Fig. 3a-b). We next asked how Ccn1l1 drives epithelial budding. CCN
173 proteins regulate cell behaviors such as adhesion, proliferation, and ECM production
174 through their conserved domains[33–35]. Zebrafish Ccn1l1 exhibits high similarity to human

175 CCN1, supporting a conserved function (Extended Fig. 3a-b). We hypothesized that bud
176 formation failure in *ccn1l1* knockdown embryos results from a loss of HA and Versican
177 synthesis. Consistent with this, *has3* and *vcanb* colocalized with *ccn1l1* at canal-genesis
178 zones (Extended Fig. 3c) and exhibited nearly identical temporal expression patterns,
179 with low expression during bud initiation, peaking during bud extension, and returning to
180 baseline during bud fusion, as previously reported[10,11,15] (Extended Fig. 3d). Indeed,
181 *ccn1l1* knockdown reduced *has3* and *vcanb* expression to background levels at the pre-
182 budding stage and by 50.1% and 73.5%, respectively, at bud extension (Fig. 3c-d and
183 Extended Fig. 3e-f). We conclude that Ccn1l1 drives bud initiation and extension by
184 promoting *has3* and *vcanb* transcription.

185 Given the HA-rich bud-ECM's role in Yap activation and *ccn1l1*'s role in HA production,
186 we hypothesized the existence of a positive feedback loop: *ccn1l1* expression triggers HA
187 production, generating ECM swelling that activates Yap, which in turn enhances *ccn1l1*
188 expression. This predicts that disrupting any component of this loop will affect the others.
189 First, we tested whether disrupting the mechanical force from ECM expansion would
190 affect gene expression. Consistent with our prediction, HAase treatment during bud
191 extension suppressed *ccn1l1* expression to pre-budding levels (Fig. 3e-f) and similarly
192 reduced *has3* expression (Fig. 3g-h). Second, we disrupted transcriptional regulation
193 using a heat-shock inducible dominant-negative (DN) Yap mutant lacking the TEAD-
194 binding domain[36], preventing the conversion of mechanical cues into transcriptional
195 outputs. These mutants showed significantly reduced bud extension and bud-ECM
196 volume (Fig. 3i-k), confirming that Yap's transcriptional activity is required for sustained
197 ECM production and morphogenesis.

198 Together, these complementary approaches, disrupting the mechanical arm with HAase
199 and blocking the transcriptional arm with dominant-negative Yap, demonstrate a positive
200 feedback loop where Ccn1l1 promotes ECM synthesis, ECM expansion activates Yap,
201 and Yap enhances *ccn1l1* expression (Fig. 3l). This creates a self-amplifying system that
202 can drive ECM expansion and bud extension from initially small signals. We next
203 examined the spatiotemporal dynamics of this feedback loop in the growing bud.

204 **Mechanical patterning of cells at the bud border sustains extension for timely bud**
205 **fusion**

206 While cell proliferation and convergence-extension through cell rearrangement are typical
207 behaviors underlying tissue growth during development, we previously showed that
208 neither is necessary for bud extension[10]. To determine the source of cells contributing to
209 this bud extension and the role of the Yap-ECM loop, we performed time-lapse imaging
210 and cell tracking. We observed a linear increase in bud cell number over time (Fig. 4a),
211 driven by cells adjacent to the bud that moved toward the initiated bud, turned along the
212 border, and became incorporated into the extending structure (Fig. 4b and Extended
213 Movie 1). Disruption of ECM expansion with HAase treatment or mechanotransduction
214 with *yap1* MO inhibited this increase in cell number (Fig. 4c-d). This suggests that, rather
215 than proliferation, ECM expansion through mechanotransduction exerts pulling forces
216 that recruit adjacent cells into the growing bud.

217 Because recruitment occurs specifically at the bud border, we hypothesized that
218 mechanotransduction cues are spatially patterned rather than uniform. To explore this,
219 we developed a theoretical vertex model of a 2D epithelial section incorporating
220 experimentally established parameters[10]: apical, lateral, and basal cellular tensions; BM
221 adhesion at the bud border; HA-rich bud-ECM pressure; and anisotropic cytocinch
222 tension orthogonal to the bud's long axis (Fig. 4e and Extended Fig. 4a-d; see
223 Supplementary Note). The model defines four mechanically distinct regions: bud-adjacent
224 cells (BM-attached), bud border cells (partially BM-attached), budding cells (newly
225 incorporated, BM-detached), and tip cells (leading-edge, BM-detached) (Fig. 4e).

226 The model indicated that cell recruitment was accompanied by a transient increase in cell
227 aspect ratio (Fig. 4f), with stronger overshoots in border and budding cells compared to
228 tip cells. This spatial pattern was lost when BM attachment or cytocinches were removed
229 (Extended Fig. 4a-d), suggesting that mechanical stress is concentrated at the border
230 cells attached to the BM. To test this prediction, we measured nuclear aspect ratios as
231 markers of cell deformation[37,38] and found that border and budding cells were more
232 deformed than tip cells (Fig. 4g and Extended Fig. 4e). Long-term time-lapse imaging of

233 the Yap reporter with a nuclear marker confirmed model predictions: cells experienced
234 significant deformation as they flowed toward and turned the bud border, concomitant
235 with strong Yap activation before recruitment (Fig. 4h-i', Extended Fig. 4f-g, and Extended
236 Movie 2). Moreover, Yap activation occurred sequentially, with each newly arriving
237 adjacent cell activating Yap as it turned the bud border (Fig. 4h and Extended Movie 2).
238 In contrast, nuclear deformation and Yap activity remained low in tip cells (Fig. 4g-i' and
239 Extended Fig. 4f-g). Notably, *ccn1l1* expression was slightly lower in border cells than in
240 budding cells, consistent with recent Yap activation (Fig. 2d), and its expression domain
241 expanded over time as additional cells were recruited into the extending bud (Extended
242 Fig. 4h-i). Together, these results demonstrate that Yap activitation is spatially restricted
243 to the bud borders and temporally dynamic, with border cells activating Yap and *ccn1l1*
244 expression as they turn the bud corner and are recruited into the bud.

245 To test the functional significance of spatially patterned mechanotransduction, we
246 modeled bud growth dynamics in which ECM production comprised two components: a
247 constant baseline rate from pre-patterned tip cells and a mechanotransductive
248 contribution proportional to the number of recruited cells. When mechanotransduction
249 strength is high, the model predicts accelerated, non-linear ECM volume growth (Fig. 4j).
250 In contrast, disabling the mechanotransductive contribution, resulted in a slower, more
251 linear increase in ECM volume consistent with constant ECM production from tip cells
252 alone (Fig. 4j). Because bud extension in the model depends on ECM volume growth,
253 reduced ECM production without mechanotransductive contribution led to slower
254 extension rates (Fig. 4l). As predicted by the model, control embryos exhibited rapid ECM
255 growth and faster extension compared to *yap1* MO-injected embryos that showed slower
256 ECM growth and reduced bud extension (Fig. 4k and 4m).

257 Extending buds eventually meet and fuse to form pillars, completing otic vesicle
258 remodeling and canal demarcation. We next examined how varying extension rates, set
259 by ECM produced by tip cells and by the mechanotransductive recruitment of neighboring
260 cells, determine whether buds achieve fusion. To address this, we generated a phase
261 diagram from ~500 simulations varying both parameters, with fusion defined as buds
262 reaching 30 μm in length (Fig. 4n), which corresponds to the average distance required

263 for opposing buds to make contact across the otic vesicle lumen in wild-type embryos at
264 60 hpf (Extended Fig. 5a). The simulations revealed a trade-off: when
265 mechanotransduction strength was low, fusion was delayed and required high tip cell
266 contribution, whereas with high mechanotransduction, even minimal tip cell production
267 was sufficient for bud fusion (Fig. 4n and Extended Fig. 4j). To test these predictions
268 experimentally, we performed dose-dependent MO-knockdowns of *ccn1l1* (Fig. 4o-p and
269 Extended Fig. 4k), which affects both tip cell and mechanotransductive ECM production.
270 At lower doses, extension slowed significantly, but buds still fused successfully by 72 hpf
271 (Fig. 4o-p). At the highest dose, extension dropped below ~95% of normal rates (Fig. 4o)
272 and buds failed to fuse (Fig. 4p). Thus, mechanotransduction ensures that buds can still
273 achieve fusion across a wide range of tip cell output, with failure occurring only under the
274 most severe loss of ECM production.

275 Our theoretical model and experimental data demonstrate that mechanical deformation
276 at bud borders activates Yap to drive cell recruitment and ECM expansion, sustaining bud
277 extension rates that ensure successful fusion even when tip cell ECM production varies.

278 **CREB activation during fusion terminates the positive feedback loop**

279 Intriguingly, *ccn1l1* expression dropped sharply once opposing buds fused (Fig. 2c and
280 2e). Consistent with this downregulation, both cell recruitment and bud extension
281 plateaued when bud pairs made contact (Fig. 4a and Extended Fig. 5a), indicating a self-
282 termination mechanism that stops further bud growth. A likely candidate for this stop
283 signal is Gpr126 (Adgrg6), a mechanosensitive adhesion-type G-protein-coupled
284 receptor (aGPCR) essential for bud fusion[15,39,40] and expressed in budding cells
285 throughout morphogenesis[15] (Extended Fig. 5b). Consistent with previous findings[15], in
286 *gpr126*$^{st49/st49}$ mutants, which carry a premature stop codon[41], buds fail to fuse and
287 undergo excessive elongation, accompanied by persistent *has3* expression (Fig. 5a-c and
288 Extended Movie 3). We found that *ccn1l1* expression remained persistently elevated in
289 these mutants at both 60 hpf and 72 hpf, contrasting with the normal sharp
290 downregulation upon fusion (Fig. 5b-c and Extended Fig. 5c) . This persistent expression
291 drove continued growth: mutant buds were 78.7% longer and contained 76.5% more cells

292 than wild type at 60 hpf (Fig. 5d-e). Notably, bud-ECM volume continued to grow
293 unchecked, with a 464.6% increase in volume (Fig. 5f and Extended Fig. 5d), consistent
294 with the ongoing recruitment of HA-producing cells. This behavior is inconsistent with a
295 genetically predetermined bud cell number, which would have produced a plateau in
296 extension. Instead, this provides further evidence that mechanotransduction recruits new
297 cells to the bud. The 2D vertex model recapitulated this behavior: when fusion was
298 blocked and the mechanotransductive contribution proportional to recruited cells allowed
299 to persist, ECM volume expanded unchecked (Extended Fig. 5e). These results
300 demonstrate that bud fusion provides the essential termination signal for the positive
301 feedback loop; in its absence, mechanotransductive recruitment drives runaway growth.

302 We next investigated how Gpr126 terminates *ccn1l1* expression. Gpr126 activates the
303 cyclic adenosine monophosphate (cAMP) pathway[42,43]. Pharmacological cAMP elevation
304 with forskolin[44] strongly reduced both *ccn1l1* and *has3* expression (Extended Fig. 5f-g)
305 and inhibited bud elongation (Extended Fig. 5h-i). Since cAMP signals through Protein
306 Kinase A (PKA), which leads to phosphorylation and activation of the transcription factor
307 CREB[45], we examined CREB activation during bud fusion. Immunostaining revealed
308 striking CREB phosphorylation at bud-bud contact sites, spreading into budding cells that
309 form the pillar (Fig. 5g). This CREB phosphorylation was absent in *gpr126* mutants (Fig.
310 5h), demonstrating that Gpr126 signaling mediates the phosphorylation of CREB.

311 CREB has been reported to downregulate CCN gene transcription in cultured cells[46,47].
312 To confirm the role of CREB in the inhibition of *ccn1l1*, we expressed DN-PKA lacking the
313 cAMP-binding site[48]. This attenuated CREB phosphorylation and prevented both bud
314 fusion and *ccn1l1* downregulation (Fig. 5i-j and Extended Fig. 5j-k), demonstrating that
315 PKA-CREB signaling is necessary for feedback termination.

316 Together, these results demonstrate that the Gpr126-cAMP-PKA-CREB pathway
317 suppresses *ccn1l1* and terminates ECM synthesis during bud fusion. This creates a
318 morphological transition-triggered, self-limiting mechanism where the successful
319 completion of morphogenesis (fusion) terminates the positive feedback loop (Fig. 5k).

Discussion

Our findings reveal how robust SCC morphogenesis emerges from a self-limiting positive feedback mechanism where morphological success triggers its own termination (Fig. 5k). We demonstrate that the mechanotransducer Yap, activated by a HA-rich ECM, drives the expression of the matricellular protein Ccn1l1, which further promotes HA and Versican synthesis to sustain ECM expansion and bud extension. This positive feedback loop is spatially restricted, with Yap activity high at the bud border. Critically, the Gpr126-cAMP-PKA-CREB pathway is activated during bud fusion and terminates *ccn1l1* expression, preventing runaway growth. Thus, the completion of morphogenesis serves as the signal to terminate the very process that drives it.

Most studies of Yap/Taz mechanotransduction have emphasized their role in negative feedback loops that maintain tissue homeostasis, where mechanical forces activate Yap/Taz to promote behaviors that ultimately dissipate those same forces[28,49–51]. More recently, however, it has become clear that Yap/Taz can also participate in positive feedback loops[52] to amplify mechanical cues rather than inhibiting them. Here we show that Yap activation promotes ECM synthesis, which generates mechanical forces that further sustain Yap activtity to generate self-reinforcing growth dynamics. We propose that this positive feedback mechanism may be important during developmental windows where weak initial signals must be robustly amplified to drive rapid morphogenetic outcomes.

The identification of Ccn1l1 as a key mediator linking Yap activation to ECM production represents a significant advance in understanding how CCN proteins contribute to mechanotransduction networks. While CCN family proteins have been implicated in developmental processes, wound healing, and inflammation[21–23], their specific role in creating positive feedback loops between mechanical forces and matrix synthesis has not been previously demonstrated. The two-stage regulation of Ccn1l1—initial Lmx1b-dependent expression followed by Yap-dependent amplification—suggests an elegant mechanism for transitioning from developmental patterning to mechanically-driven growth amplification. Notably, *ccn1l1* is also expressed in other organs, including somite and

349 notochord[21], raising the possibility that similar feedback-driven mechanisms operate more
350 broadly during vertebrate development.

351 CCN proteins are known to interact with integrins to regulate ECM production[33–35], and
352 among them, β1 integrin is a well-documented receptor for CCN family members[26,34,53].
353 β1 integrin expression has indeed been reported in the OV of both zebrafish and mice[54,55],
354 suggesting that *ccn1l1* may act via integrin to promote ECM production during SCC
355 formation. Beyond ECM regulation, CCN proteins can also remodel the actomyosin
356 cytoskeleton through integrin-Rho GTPase signaling, thereby promoting cellular
357 protrusions and generating mechanical tension[26]. We previously reported that
358 cytocinches progressively increase during bud extension and are essential for longitudinal
359 growth[10], coinciding with the rise in *ccn1l1* expression. These observations raise the
360 possibility that *ccn1l1* not only promotes ECM expansion, but may also contribute to bud
361 extension by modulating cytoskeletal tension.

362 Our theoretical model predicts that BM attachment is crucial for spatially restricting Yap
363 activation to border cells, yet this prediction remains to be investigated. Integrins,
364 particularly those that bind laminin components of the BM[56], are prime candidates for
365 transducing mechanical forces at these sites. Focal adhesion kinase (FAK) and related
366 signaling molecules, such as vinculin, likely serve as mechanosensitive intermediates that
367 link integrin engagement to Yap activation[7]. The precise mechanical threshold required
368 for Yap activation, and how BM composition and stiffness modulate this threshold,
369 represents an important avenue for future investigation. Understanding these molecular
370 details could reveal how tissues fine-tune their mechanosensitivity during morphogenesis.

371 Adhesion GPCRs (aGPCRs) perform diverse developmental roles in many organs like
372 heart, sciatic nerve, cartilage, and vascular systems, and their dysfunction can lead to
373 organ malformation or embryonic lethality[39,57–60]. Previous work implicated Gpr126 in
374 downregulating ECM production during SCC formation[15], but the molecular mechanism
375 was unknown. We find that Gpr126 signaling is activated during fusion and terminates
376 ECM production by downregulating *ccn1l1*. Such termination mechanisms may represent
377 a conserved principle by which aGPCRs couple tissue remodeling to signaling and

transcriptional outcomes during morphogenesis. Although the precise mode of Gpr126 activation remains unclear, it likely involves ligand binding and/or mechanical forces that expose a tethered agonist (Stachel sequence) to trigger downstream signaling[61–64].

The integration of mechanotransduction feedback loops to morphological outcomes provides a framework for understanding how complex organ shapes emerge through self-organizing principles. Overall, we demonstrate how robust SCC morphogenesis emerges from an interplay of two evolutionarily conserved pathways. The mechanotransduction feedback loop, Yap-Ccn1l1-HA, drives bud extension, and the Gpr126-cAMP-PKA-CREB pathway couples bud fusion to extension termination. This principle likely applies broadly to developmental systems where patterned growth-promoting signals must first be amplified and then precisely shut down.

Materials and Methods

Animals

Zebrafish (*Danio rerio*) EK and AB wild-type strains were used in this study. Adult fish were kept on a 14-hour light/10-hour dark cycle. Embryos were collected by crossing female and male adults (3-18 months old) and raised in 28.5 °C egg water. In this study, the following transgenic and mutant lines were used: *Tg(actb2:membrane-neongreen-neongreen)*[10], *lmx1b*$^{jj410/jj410}$ [38], *Tg(hsp70l: RFP-DN-Yap1)* (this study), *Tg(hsp70l: DN-PKA-GFP)* (this study), *gpr126*$^{st49/st49}$ [41], *TgKI(Yap1-mScarlet)*^{pd1280} (this study), *Tg(actb2: H2B-EGFP)* (this study), and *Tg(βActin: utrophin-mCherry)*[65]. *gpr126*$^{st49/st49}$ mutant fish were maintained as an AB strain background, whereas all other transgenic and mutant lines were maintained as an EK strain background.

Morpholino injection

Standard control MOs and MOs targeting *ccn1l1* (5′-CTCAGAGGAGACATGGTGTTATCCA-3′, translational blocking), *yap1* (5′-AGCAACATTAACAACTCACTTTAGG-3′, splice-modifying between intron 2 and exon 2) [16], and *p53* (5′-GCGCCATTGCTTTGCAAGAATTG-3′, translational blocking)[66] were

405 purchased from Gene Tools. The *ccn1l1* MO target sequence was designed based on
406 the Danio rerio *ccn1l1* sequence (ENSDART00000051336), retrieved from the Ensembl
407 database, using the Gene Tools Oligo design service. For the *ccn1l1* knockdown,
408 embryos at the single-cell stage were injected with 2 ng of *ccn1l1* MO or control MO,
409 together with 1 ng of *p53* MO. For the *yap1* knockdown, 5 ng of *yap1* MO was injected
410 with 2.5 ng of *p53* MO into embryos at the single-cell stage. MO-injected embryos were
411 screened for inner ear phenotype at 40-50 hpf and used for confocal live imaging, HCR-
412 FISH, or immunostaining at 40-72 hpf. To test the dose-dependent effect of *ccn1l1* MO,
413 embryos at the single-cell stage were injected with either standard control MO (2 ng) or
414 *ccn1l1* MO (0.5, 1, or 2 ng), together with *p53* MO. Injected embryos were screened for
415 inner ear phenotype at 50 hpf, followed by confocal live imaging at 50, 56, and 72 hpf.
416 *p53* MO was co-injected with control, *ccn1l1* or *yap1* MO to reduce MO-injection induced
417 apoptosis and non-specific toxity.

418 **Genome editing by CRISPR-Cas9**

419 *ccn1l1* CRISPANT embryo

420 Single-guide RNAs (sgRNAs) were synthesized as previously reported[11]. Briefly, sgRNAs
421 targeting multiple coding regions of *ccn1l1* were synthesized using MEGAscript SP6
422 Transcription Kit (Invitrogen, AM1330) and purified with RNA Clean & Concentrator kit
423 (Zymo Research, R1018). For the knockdown of *ccn1l1*, three sgRNAs were pooled
424 together and injected into embryos as previously described[11]. Briefly, embryos at the
425 single-cell stage were injected with 2 nL of injection solution containing pooled sgRNAs
426 (200 ng/μL: 66.6 ng/μL of each sgRNA) and Cas9 protein (PNA Bio, CP-03, 500 ng/μL).
427 F0 crispant embryos were screened for inner ear phenotype at 50-72 hpf and then used
428 for HCR-FISH or confocal live imaging. The following target sites were used to generate
429 sgRNAs: *ccn1l1* sgRNA1: 5'-CGGCGGGCACAGCGCCAGTCGGG-3'; *ccn1l1* sgRNA2:
430 5'-GTGTGTCCTCAGGTGCAGGGAGG-3'; *ccn1l1* sgRNA3: 5'-
431 AGGTGGCTGGAGCGATAGGGCGG-3'

432 *tyrosinase* CRISPANT embryo

433 A sgRNA targeting the *tyrosinase* gene[67] was synthesized as described above. sgRNA
434 (200 ng/μL) and Cas9 protein (500 ng/μL) were injected into embryos at the one-cell stage
435 as described above. The *tyrosinase* crispant embryos were screened for pigmentation
436 loss at 50-72 hpf and used for HCR-FISH or confocal live imaging. *tyrosinase* crispant
437 embryos were used as an sgRNA injection control, resulting in loss of pigmentation
438 without affecting SCC formation[11]. The following target site was used to generate the
439 sgRNA: 5′-GGACTGGAGGACTTCTGGGG-3′.

440 Generation of *TgKI(Yap1-mScarlet)* line

441 The *TgKI(Yap1-mScarlet)*^{pd1280} line was generated using a previously reported knock-in
442 tagging method[14]. As the targeting cassette, a gene fragment spanning from the middle
443 of intron 7 to the last codon of exon 8 was cloned into pUC19-TgKI-MCS-mScarlet-MCS-
444 polyA (Addgene plasmid #174023) using In-Fusion seamless cloning (Takara Bio) with
445 the following primers: *yap1* Fw: 5′-
446 TTCGCTAGCCCGCGGCTATCAGTGCTTTACAGATCATTGTC-3′; *yap1* Rev: 5′-
447 CACCTCGAGTCTAGATAGCCAGGTTAGAAAGTTCTCC-3′. The sgRNA target sites for
448 genomic editing were mutated in the donor plasmid using Q5 site-directed mutagenesis
449 (New England Biolabs, NEB) with the following primers: *yap1* SDM Fw: 5′-
450 ACATCCTCAACGACATGGAGTCAGTGCTGGC-3′; *yap1* SDM Rev: 5′-
451 CGGAGCTCAAAGCTTCCTGCAGGCTGGGCA-3′. A sgRNA targeting *yap1* (5′-
452 GTTGAGGATGTCGGAGCTTAGGG-3′) was synthesized using the HiScribe T7 Quick
453 High Yield RNA Synthesis Kit (NEB) and purified with the Monarch RNA Cleanup Kit
454 (NEB). The injection mix contained PCR donor (20 nM), gRNA (4 μM), Cas9 protein (3
455 μM; PNA Bio CP-02), and DMSO (1%). The genomic integration site was confirmed by
456 sequencing at the F2 generation, and the line was designated allele number pd1280.

457 **Construct the generation and injection of plasmid and mRNA**

458 *actb2:H2B-EGFP* plasmid

459 H2B-EGFP was amplified by PCR using Phusion Flash High-Fidelity PCR Master Mix
460 (Thermo Fisher Scientific, F548L) and appropriate primers from a construct harboring its

461 coding sequence. pMTB *actb2:membrane-neongreen-neongreen* construct[10], which
462 contains the SP6 promoter for mRNA synthesis, was used as the plasmid backbone. The
463 plasmid backbone was digested with BamHI and AgeI. Then, the amplified H2B-EGFP
464 fragment was cloned downstream of the *actb2* promoter and the SP6 promoter in the
465 pMTB backbone using In-Fusion Snap Assembly Master Mix (Takara, 638948). The H2B-
466 EGFP mRNA was synthesized using the mMESSAGE mMACHINE SP6 transcription kit
467 (Invitrogen, AM1340) from the linearized *actb2:H2B-EGFP* plasmid. 2 nL of mRNA (100
468 ng/μL) was injected into single-cell-stage embryos from *TgKI(Yap1-mScarlet)* parents.
469 Live embryos were observed at 40-56 hpf by confocal microscopy. To generate the
470 *Tg(actb2:H2B-EGFP)* line, 100 pg of Tol2 mRNA and 50 pg of *actb2:H2B-EGFP* plasmid
471 were injected into embryos at the one-cell stage. The following primers were used for
472 PCR: Fw: 5'-CTTGTTCTTTTTGCAGGATCCCGCCACCATGCCAGAGCCAGCGA-3';
473 Rev: 5'-TTATCATGTCTGGATCACCGGTTTACTTGTACAGCTCGTCCATGC-3'.

474 *hsp70l: RFP-dominant negative Yap1* plasmid

475 *hsp70l: RFP-DN-Yap1*[36] construct harboring the I-Sce Ⅰ site for the transgene was a gift
476 from Kenneth Poss (Morgridge Institute, University of Wisconsin-Madison, USA) and was
477 used as a template for cloning. RFP-DN-Yap1 was amplified by PCR using appropriate
478 primers. The plasmid backbone, which contains a heat-shock-inducible promoter (hsp70l)
479 and Tol2 sites, was digested with BamH1 and AgeI and then gel-purified. The amplified
480 DNA fragment was cloned downstream of the *hsp70l* promoter in the plasmid backbone
481 using the In-Fusion system. To generate the *Tg(hsp70l: RFP-DN-Yap1)* line, 100 pg of
482 Tol2 mRNA and 50 pg of *hsp70l: RFP-DN-Yap1* plasmid were injected into embryos at
483 the one-cell stage. The following primers were used for PCR: Fw: 5'-
484 TTGCAGGATCCGCCACCATGGACAACACCGAGGACG-3'; Rev: 5'-
485 TGGATCACCGGTTCAGATACTACTGTGGGCTGGAGGG-3'

486 *hsp70l: dominant negative PKA-GFP* plasmid

487 M7 pdnPKA-GFP was a gift from Randall Moon (Addgene plasmid # 16716), used as a
488 template for cloning. The cloning was performed, as described above. Briefly, the

489 amplified dnPKA-GFP fragment was cloned downstream of the *hsp70l* promoter in the
490 plasmid backbone. To generate the *Tg(hsp70l: DN-PKA-GFP)* line, 100 pg of Tol2 mRNA
491 and 50 pg of *hsp70l: DN-PKA-GFP* plasmid were injected into embryos at the one-cell
492 stage. The following primers were used for PCR: Fw: 5'-
493 TACAGTTCAGCCATCCTAGGATTTAGGTGACACTATAGAATACAAGCTACT-3'; Rev:
494 5'-GTTCCGGATACGTATGAATTCTTATTTGTATAGTTCATCCATGCCATGT-3'

495 **Drug treatment**

496 For hyaluronidase treatment, we injected hyaluronidase (HAase, Sigma Aldrich, H1136)
497 into the periotic space of dechorionated embryos, with slight modifications to a previously
498 reported method[10]. Briefly, HAase (500 units/mL) was injected into embryos twice at a 3-
499 hour interval from 46 hpf, followed by HCR-FISH or confocal live imaging. For live imaging
500 of *TgKI(Yap1-mScarlet)* embryos, HAase was injected into embryos at 50 hpf, followed
501 by imaging at 1.5 hours post-injection. For immunostaining of Yap1 antibody, HAase was
502 injected into embryos at 50 hpf, and embryos were fixed with 4% PFA in PBS at 3 hours
503 post-injection, followed by immunostaining. For RO4929097 (ApexBio, A4005) treatment,
504 dechorionated embryos at 24 hpf were soaked in egg water containing 50 μM inhibitor for
505 26 hours, followed by HCR-FISH. For forskolin (Cayman Chemical, 1101810) treatment,
506 dechorionated embryos were soaked in egg water containing 50 μM of the drug at 46 hpf
507 for 6 hours, followed by HCR-FISH or confocal live imaging.

508 **Multiplex *in situ* hybridization chain reaction (HCR)**

509 HCR probes for each gene were obtained from IDT (Oligo Pools, oPools). Hybridization
510 buffer, amplification buffer, wash buffer, and amplifiers were purchased from Molecular
511 Instruments. mRNA sequences used for HCR probe design were retrieved from the NCBI
512 database. HCR probe sets for each mRNA were designed using a home-made Python
513 script[31]. 40 probe oligonucleotides targeting each mRNA were generated and pooled
514 oligonucleotides were used for HCR-FISH. HCR probe sequences are listed in
515 Supplementary Table 1. HCR-FISH experiments were performed as previously
516 described[10,11]. Dechorionated embryos at various stages were fixed with 4%

517 paraformaldehyde (PFA) in PBS and permeabilized with prechilled acetone. The embryos
518 were then incubated with the hybridization buffer at 37°C for 30 min, followed by
519 incubation with the hybridization solution containing probes overnight at 37°C. After probe
520 hybridization, the embryos were incubated overnight at room temperature in an
521 amplification buffer with fluorescent HCR amplifiers (Alexa-488, Alexa-546, or Alexa-647).
522 Embryos were washed four times with 0.1% Tween-20 in 5× SSC buffer (5x SSCT) and
523 stored in 1x PBS at 4°C until confocal imaging. For nuclear staining, HCR-FISH stained
524 embryos were incubated with Hoechst 33342 (Thermo Fisher Scientific, 62249; 1:2000)
525 at 4°C overnight, followed by washing with 1x PBS. Control and experimental samples
526 were processed within the same tube to ensure uniform treatment. This included the
527 same incubation times, reagent concentrations, and handling procedures, ensuring that
528 any differences in fluorescence intensity were due to variations in target abundance rather
529 than experimental variability.

530 **Immunohistochemistry**

531 Immunohistochemistry was performed as previously described[11]. Briefly, for phospho-
532 CREB staining, the dechorionated embryos were fixed with 4% PFA/PBS for 2 hours at
533 room temperature, followed by permeabilization with pre-chilled acetone at -20 °C for 7
534 minutes. Embryos were then blocked with 5% bovine serum albumin (BSA; Sigma-Aldrich,
535 A3311) in 1× PBS containing 0.1% Tween-20 (PBT) at room temperature for 1 h, followed
536 by incubation in primary antibody solution containing rabbit anti-phospho-CREB (Ser133)
537 antibody (Cell Signaling Technology, 9198; 1:100) and mouse anti-GFP antibody
538 (Invitrogen, A11120; 1:500) at 4°C overnight. Embryos were washed with 1x PBT for 5
539 min, thrice, then incubated with a secondary antibody solution containing fluorescently
540 labeled anti-rabbit and anti-mouse antibodies (Thermo Fisher Scientific, A11008, A11035,
541 A21244, and A11001; 1:200) and phalloidin (Thermo Fisher Scientific, A22287; 1:100) at
542 4°C overnight. Embryos were washed with 1x PBT for 5 min, thrice, and stored at 4°C.
543 For Yap1 staining, embryos fixed with 4% PFA/PBS were permeabilized with 2% Triton
544 X-100/PBS for 2 hours. Embryos were then blocked with 2% BSA in 1× PBS containing
545 1% DMSO and 0.1% Triton X-100 (PBDT) for 2 hours at room temperature, followed by
546 incubation in a primary antibody solution containing rabbit anti-Yap1 (Proteintech, 13584-

547 1-AP; 1:200) at 4 °C overnight. Embryos were washed with 1× PBDT for 15 min, thrice,
548 then incubated with a secondary antibody solution containing fluorescently labeled anti-
549 rabbit antibody (1:200) and Hoechst 33342 (1:2000) at 4°C overnight. Following this,
550 embryos were washed with 1× PBDT for 15 minutes, thrice.

551 **Confocal imaging**

552 Confocal imaging was performed with a Zeiss LSM 980 confocal microscope using a C-
553 Apochromat 40×1.2 NA objective for all fluorescence acquisitions as previously
554 described[11]. Briefly, dechorionated live embryos were anesthetized in 1x tricaine and then
555 mounted dorsolaterally using a canyon mount cast in 1.5% agarose dissolved in egg
556 water and covered with a coverslip. Images of *TgKI(Yap1-mScarlet)* embryos were
557 acquired using Airyscan SR mode, followed by image processing using the Zen software
558 (Zeiss). For imaging embryos stained with HCR-FISH or immunohistochemistry, embryos
559 were mounted on 1.5% agarose dissolved in 1x PBS and then subjected to confocal
560 imaging. Image acquisition settings, such as laser power, gain, and exposure, were kept
561 constant and within the sub-saturation range during microscopy to allow for accurate and
562 quantitative sample comparisons. Time-lapse imaging was performed as previously
563 described[10]. Briefly, embryos were immobilized by injecting 500 μM α-bungarotoxin
564 protein in PBS (Thermo Fisher Scientific, B35450) into the heart 30 min before imaging.
565 The embryos were maintained in a custom-built incubator at 28.5°C during time-lapse
566 imaging. Z-stack images were acquired at 30-minute intervals. For time-lapse analysis of
567 Yap1 nuclear translocation, posterior buds of *TgKI(Yap-mScarlet); Tg(actb2:H2B-EGFP)*
568 embryos were used. Z-stack Images were acquired from 54 hpf at 1 hour intervals with
569 Airyscan Multiplex mode (CO-8Y) for fast scanning, which enabled high-speed imaging
570 with enhanced spatial resolution while reducing excitation dose to minimize
571 photobleaching. Acquired images were processed using Zen software. FluoRender, an
572 open-source software[68], was used for 3D renderings of images.

573 **Screening and genotyping of mutants**

574 *gpr126* $^{st49/49}$ mutants, derived from *gpr126* $^{st49/+}$ parents, were screened based on inner
575 ear phenotypes at 60 hpf[15] for immunohistochemistry . For Fig. 5a–f and Extended Fig.
576 5c-d, EK wild-type and *gpr126* $^{st49/49}$ mutants were obtained from EK wild-type and *gpr126*
577 $^{st49/49}$ parents, respectively, and subsequently subjected to HCR-FISH and confocal live
578 imaging at 50-72 hpf. To minimize developmental differences between mutant and wild-
579 type embryos, male and female fish were maintained in a mating tank separated by a
580 removable divider overnight, and fertilized eggs were collected within 15 minutes after the
581 divider was removed the following morning. *lmx1bb* $^{jj410/+}$ mutants were genotyped using
582 the derived cleaved amplified polymorphic sequence (dCAPS) method, as previously
583 described[11]. The *lmx1bb* $^{jj410/jj410}$ mutant obtained from *lmx1bb* $^{jj410/+}$ parents was screened
584 based on inner ear phenotypes at 50 hpf, followed by HCR-FISH.

585 **Heat-shock activation of hsp70l promoter**

586 For experiments using DN-Yap1 mutants, *Tg(Hsp70l: RFP-DN-Yap1)* fish were crossed
587 with *Tg(actb2:membrane-neongreen-neongreen)* fish. Embryos obtained from this cross
588 were heat-shocked at 37°C for 30 min twice at 5-hour intervals at 40 hpf, followed by
589 confocal live imaging at 50 hpf. DN-Yap1 mutants were identified by RFP fluorescence at
590 5 hours post-heat shock. RFP-negative siblings were used as controls for confocal
591 imaging. For experiments using DN-PKA mutants, *Tg(Hsp70l: DN-PKA-GFP)* fish were
592 crossed with wild-type or *Tg(βActin:utrophin-mCherry)* fish. To induce acute activation of
593 the heat-shock promoter before bud fusion, embryos were heat-shocked at 42°C for 10
594 min at 48 hpf, followed by HCR-FISH or confocal live imaging at 56 hpf. DN-PKA mutants
595 were identified by GFP fluorescence at 3 hours post-heat shock. GFP-negative siblings
596 were used as controls for HCR-FISH or confocal live imaging. Heat-shock treatment at
597 42°C for 10 min was confirmed not to affect zebrafish embryonic development noticeably.

598 **Modeling**

599 See Theory Supplementary Note

600 **Analysis of single-cell RNA sequencing data**

601 Single-cell RNA sequencing analysis was performed using
602 Daniocell2023_SeuratV4.rds[19,20] available at https://daniocell.nichd.nih.gov/. The
603 published Seurat object was processed in R (v 4.4.0) using Seurat (v5.2.1)[69]. The R script
604 of this analysis can be obtained at GitHub (https://github.com/MunjalLab/ccn1l1_project).
605 Clusters of otic tissue cells from 36 hpf to 72 hpf were isolated from the original Daniocell
606 atlas. 3000 highly variable genes were selected using the Seurat function
607 'FindVariableFeatures' with the method 'vst'. All genes were then scaled to have a mean
608 expression of 0 and a variance of 1 across all selected cells. Clustering was performed
609 using the Louvain algorithm[70] implemented in FindClusters with a resolution of 0.6. The
610 canal-forming cell cluster was identified based on expression of *vcanb*, a known marker
611 for this cell type, supported by previous literature[11,15]. The top 10 differentially expressed
612 genes were identified by the 'FindAllMarkers' function in Seurat.

613 **Comparative analysis of Ccn1l1 and Ccn1 amino acid sequences**

614 For the analysis of the functional domains of zebrafish Ccn1l1, amino acid sequences
615 were retrieved from the NCBI database. Functional domains were predicted using the
616 SMART database[71,72], and the significance (E-value) of each predicted domain was
617 recorded. To compare domain conservation across species, multiple sequence
618 alignments were performed using Clustal Omega[73], and sequence similarity and percent
619 identity were assessed. Clustal alignment outputs were used to visualize conserved
620 residues, and the pairwise identity matrix was used to quantify percent identity between
621 species. Amino acid sequences of each functional domain predicted by SMART are listed
622 in Supplementary Table 2.

623 **Analysis of the TEAD-binding domain in 5' upstream region of *ccn1l1***

624 For this analysis, genomic DNA was extracted from EK wild-type embryos at 2 dpf, and
625 a 7-kb fragment of the 5′ upstream region of *ccn1l1* was amplified by PCR. The sequence
626 of the PCR product was determined by Sanger sequencing and analyzed for the presence
627 of the TEAD-binding motif (GGAATG/CATTCC)[24,28–30]. The following primers were used

628 for PCR: forward, 5′- TATGTCAAACACACAAGCAGTGG-3′; reverse, 5′-
629 GGTGTTATCCAAAAAATTGTTAAGAGGC-3′.

630 **Quantification and statistical analysis**

631 The majority of image analysis was performed in Fiji[74], unless otherwise noted.

632 **1) Bud length measurement**

633 For quantification, images were acquired by confocal live imaging of *Tg(actb2:membrane-*
634 *neongreen-neongreen*) embryos, with z-stacks collected at 0.5 or 1 μm intervals. 2D
635 images capturing the middle section of the bud were used to measure the bud length of
636 embryos. Bud lengths were measured manually using the "straight-line" tool in Fiji. Where
637 budding had not started or in perturbations where budding was affected, bud lengths
638 correspond to average cell height at the anterior or posterior region. For time-lapse
639 analysis, the same buds were tracked every 30 min, and the bud length was measured
640 at each time point. For the anterior bud length of *gpr126*$^{st49/st49}$ mutants or the anterior
641 pillar of WT embryos (Fig. 5), bud length was measured by Imaris software. Using the
642 "spot" tool, spots were placed along the centerline of the bud, and the total length was
643 calculated by connecting these spots.

644 **2) Cell and nuclear aspect ratio**

645 The cell aspect ratio of budding cells was measured using the "Straight-Line" tool in Fiji.
646 Z-stack images of the OV in *Tg(actb2:membrane-neongreen-neongreen*) embryos were
647 acquired by confocal live imaging at 0.5 μm intervals. 2D images capturing the middle
648 section of budding cells were used to measure cell height and width, as shown in
649 Extended Fig. 1a. For time-lapse analysis, the same cells were tracked every 30 min, and
650 the cell aspect ratio was measured at each time point. To measure the 3D nuclear aspect
651 ratio (Fig. 4g), embryos were injected with H2B-EGFP mRNA, followed by confocal live
652 imaging at 50 hpf. Z-stack images of anterior buds were acquired at 0.5 μm intervals. The
653 3D nuclear aspect ratio was measured using Imaris. Using the "Surface" tool, masks
654 delineating the H2B-EGFP signal were generated at 1 μm intervals in the 3D images and

655 subsequently merged to reconstruct an ellipsoidal 3D nuclear model, as shown in
656 Extended Fig. 4e. The lengths of the long and short axes of the ellipsoid were quantified,
657 and the nuclear aspect ratio was calculated. For time-lapse analysis of the 2D nuclear
658 aspect ratio (Fig. 4i' and Extended Fig. 4f), Z-stack images of the OV in *TgKI(Yap1-*
659 *mScarlet); Tg(actb2:H2B-EGFP)* embryos were acquired by confocal live imaging at 1 μm
660 intervals. 2D images capturing the middle section of cell nuclei were used to measure
661 nuclear height and width, and the 2D nuclear aspect ratio of individual cells was tracked
662 at 1 hour intervals

663 **3) Counting cell numbers in a bud**

664 Cell counting was performed using the Mastodon plugin (https://github.com/mastodon-
665 sc/mastodon) in Fiji, which enables 3D image analysis. 3D z-stack images of the otic
666 vesicle in *Tg(actb2:membrane-neongreen-neongreen*) embryos were acquired by
667 confocal live imaging at 0.5 or 1 μm slice intervals. Using the Big Data Viewer in the
668 Mastodon plugin, all cells in a bud were manually marked in 3D and counted. For time-
669 lapse analysis, the same buds were tracked every 30 min, and the cell number was
670 counted at each time point. For counting the *ccn1l1-expressing* cells, Z-stack images of
671 OV in embryos stained with HCR-FISH probe against *ccn1l1* and Hoechst 33342 were
672 used. The number of *ccn1l1*-expressing cells was quantified counted by Imaris "spot " tool.

673 **4) Bud-ECM volume measurement**

674 The bud-ECM region was defined as shown in Extended Fig. 1a. 3D z-stack images of
675 the otic vesicle in *Tg(actb2:membrane-neongreen-neongreen*) embryos were acquired by
676 confocal live imaging at 1 μm slice intervals. Bud-ECM volume was measured using
677 Imaris software. Using the "surface" tool, masks delineating the bud-ECM area were
678 generated at 1 μm slice intervals in the 3D images and subsequently merged to
679 reconstruct a 3D surface filling the bud-ECM region, and the volume was quantified. For
680 time-lapse analysis, the same buds were tracked every 30 min, and the volume of bud-
681 ECM region was measured at each time point.

682 **5) Intensity analysis of multiplex *in situ* HCR (HCR-FISH)**

683 Measurement of the fluorescence intensity of the HCR probes was performed as
684 previously described[11]. In brief, using Fiji, maximum intensity z-projections covering the
685 entire anterior or posterior bud were created. To measure the mean intensity of HCR
686 probes, the ROI was manually drawn along the outer cells of the bud with a "segmented
687 line" tool. To create a histogram plot of fluorescence intensity, regions of interest (ROIs)
688 were manually drawn using the "segmented line" tool (10 pixels wide) along the anterior
689 budding region, spanning 55-65 μm, as shown in Fig. 2. An additional 20 μm on each side
690 of the non-budding region flanking the budding cells was also included. The "plot profile"
691 tool was then used to obtain an average intensity trace along the line. Fluorescence
692 intensities were divided into 120 and 40 bins for the budding and shoulder regions,
693 respectively, expressed as normalized distances, and subsequently normalized again to
694 the overall maximum value. The Fire heatmap was used to represent the fluorescence
695 intensities of individual probes. The heatmap color scale was adjusted individually for
696 each experiment.

697 **6) Intensity analysis of the Yap1 nuclear-to-cytoplasm ratio**

698 For measurement of the Yap1 nuclear-to-cytoplasmic ratio in immunostained samples,
699 nuclear and cytoplasmic regions in a 2D slice at the middle section of each cell were
700 manually segmented based on Hoechst and phalloidin staining, respectively, using Fiji
701 software, and the ratio of mean nuclear to mean cytoplasmic signal intensities was
702 calculated. For measurement using the *TgKI(Yap1-mScarlet)* line, nuclei in a 2D slice at
703 the middle section of each cell were manually segmented based on the H2B-EGFP signal,
704 and the mean nuclear Yap1 signal intensity was quantified. The mean cytoplasmic Yap1
705 signal intensity was obtained on the same 2D slice using the "oval" tool in Fiji by placing
706 four circular ROIs in the cytoplasm and averaging their mean intensities. The Yap1
707 nuclear-to-cytoplasmic ratio was then calculated as described above. For time-lapse
708 analysis of Yap1 nucleae-to-cytoplasmic ratio, posterior buds of *TgKI(Yap1-mSacrlet);*
709 *Tg(actb2:H2B-EGFP)* embryos were used. The Yap1 nuclear-to-cytoplasmic ratio of
710 individual cells was tracked at 1 hour intervals as described above. To generate color-
711 coded images based on the Yap1 nuclear-to-cytoplasmic ratio, we referred to previously
712 published methods[75]. Briefly, Z-stack images of the posterior bud from *TgKI (Yap1-*

713 *mScarlet); Tg(actb2:H2B-EGFP)* embryos were reconstructed from four consecutive 2D
714 slices. Nuclear masks for individual cells in the Z-stack images were created in Fiji based
715 on the H2B-EGFP signal. The positional information of each nuclear mask was then
716 extracted, and the corresponding Yap1 nuclear-to-cytoplasmic ratio values, quantified
717 from the 2D slices, were mapped onto each nuclear mask using MATLAB to generate
718 color-coded images.

719 **Measurement of the number of embryos with unfused buds**

720 Number of embryos injected with control MO or *yap1* MO with visible unfused bud
721 morphologies by the total number of embryos measured at 72 hpf. The "unfused"
722 phenotype includes embryos with failure of fusion of all buds and those with fusion failure
723 of only the posterior and ventral buds.

724 **Statistical analysis**

725 Average values were calculated from 'n,' where 'n' represents the number of buds, bud-
726 ECM, and cells (as labeled in each figure). Plots show individual data points, mean values,
727 and error bars (standard deviation of the mean, as labeled). Before performing parametric
728 statistical tests, the Kolmogorov-Smirnov and Shapiro-Wilk tests were used to test if the
729 dataset in each experiment was from a normal distribution. To compare the difference
730 between the two groups, unpaired or paired two-tailed Student's t-tests were performed.
731 For multiple comparisons, one-way ANOVA with Tukey's test for normally distributed data
732 and Kruskal-Wallis test with Dunn's test for non-normally distributed data were performed.
733 P-values less than 0.05 were considered to be significant. All statistical tests and plots
734 were made in GraphPad Prism 10.

735 **Acknowledgments**

736 We are thankful to Nadia Eliora, Vishank Jain-Sharma, and other members of the
737 Principles of Tissue Morphogenesis (Munjal) Lab for their feedback and support. We
738 thank Brigid Hogan and Stefano Di Talia for their critical comments on the manuscript.
739 We thank Kenneth Poss for providing the *hsp70l: RFP-DN Yap1* construct. We thank

members of the Poss and Bagnat labs for valuable technical input during this project. We thank Sean Megason and Ian Swinburne for their guidance and support during AM's postdoctoral training. We thank Kazunori Ando for technical support and advice to YM. We thank Toru Kawanishi and Sean Megason for sharing the Yap immunostaining protocol. We thank Tony Tsai's lab for sharing the *Yap (4xGTIIC:EGFP)* reporter, which was not included in the final manuscript. We thank Nanami Sato for illustrations. We thank Ziqi Lu for assistance in developing the code for generating time-lapse movies of the *TgKI(Yap1-mScarlet)* line. We thank the Duke Zebrafish Core Facility of the Duke School of Medicine for their support. This work was funded by the National Institute of Child Health and Human Development (R00HD098918 and DP2115157 to A.M.) and the National Institute of Arthritis and Musculoskeletal and Skin Diseases (R01AR083346 to M.B). YM is supported by JSPS Overseas Research Fellowship, Duke Regeneration Centre Career Advancement Award, and Uehara Memorial Foundation Overseas Research Fellowship.

Author contributions

A.M. conceived and initiated the project. Y.M., with input from A.M., subsequently developed the project direction. Y.M. designed, performed, and analyzed most of the experiments with the assistance of A.M., A.B.B., and K.L.H. P.R. developed the theoretical model with the supervision of E.H. Y.M. generated the *Tg(hsp70l: RFP-DN-Yap1)* line, *Tg(hsp70l: DN-PKA-GFP)* line, *Tg(actb2: H2B-EGFP)* line, and all constructs for the project, except those required for the *TgKI(Yap-mScarlet)* line. D.S.L. and M.B. generated the *TgKI(Yap-mScarlet)* line and the corresponding construct. J.W. analyzed the publicly available transcriptomics dataset. Y.M. and P.R. prepared figures with the input from E.H. and A.M. Y.M. and A.M. interpreted the data and wrote the original manuscript with input from P.R. and E.H. All authors reviewed and edited the manuscript. A.M. acquired funding for the project. A.M. supervised and administered the project.

Declaration of interests

The authors declare no competing interests.

References

1. Hannezo, E., and Heisenberg, C.-P. (2019). Mechanochemical Feedback Loops in Development and Disease. Cell *178*, 12–25. https://doi.org/10.1016/j.cell.2019.05.052.

2. Collinet, C., and Lecuit, T. (2021). Programmed and self-organized flow of information during morphogenesis. Nat. Rev. Mol. Cell Biol. *22*, 245–265. https://doi.org/10.1038/s41580-020-00318-6.

3. Schier, A.F. (2003). Nodal signaling in vertebrate development. Annu. Rev. Cell Dev. Biol. *19*, 589–621. https://doi.org/10.1146/annurev.cellbio.19.041603.094522.

4. Moeller, M.E., Danielsen, E.T., Herder, R., O'Connor, M.B., and Rewitz, K.F. (2013). Dynamic feedback circuits function as a switch for shaping a maturation-inducing steroid pulse in Drosophila. Development *140*, 4730–4739. https://doi.org/10.1242/dev.099739.

5. Vogel, V., and Sheetz, M. (2006). Integrins and Extracellular Matrix in Mechanotransduction Martin Alexander Schwartz 3. Nat Rev Mol Cell Biol *7*, 265–275.

6. Di, X., Gao, X., Peng, L., Ai, J., Jin, X., Qi, S., Li, H., Wang, K., and Luo, D. (2023). Cellular mechanotransduction in health and diseases: from molecular mechanism to therapeutic targets. Signal Transduct. Target. Ther. *8*, 282. https://doi.org/10.1038/s41392-023-01501-9.

7. Dupont, S., Morsut, L., Aragona, M., Enzo, E., Giulitti, S., Cordenonsi, M., Zanconato, F., Le Digabel, J., Forcato, M., Bicciato, S., et al. (2011). Role of YAP/TAZ in mechanotransduction. Nature *474*, 179–183. https://doi.org/10.1038/nature10137.

8. Totaro, A., Panciera, T., and Piccolo, S. (2018). YAP/TAZ upstream signals and downstream responses. Nat. Cell Biol. *20*, 888–899. https://doi.org/10.1038/s41556-018-0142-z.

9. Combredet, C., Ansel, M., and Brunet, T. (2025). A selection-based knockout approach for a choanoflagellate reveals regulation of multicellular development by Hippo signaling. Cell Rep. *44*, 116345. https://doi.org/10.1016/j.celrep.2025.116345.

10. Munjal, A., Hannezo, E., Tsai, T.Y.-C., Mitchison, T.J., and Megason, S.G. (2021). Extracellular hyaluronate pressure shaped by cellular tethers drives tissue morphogenesis. Cell *184*, 6313-6325.e18. https://doi.org/10.1016/j.cell.2021.11.025.

11. Mori, Y., Smith, S., Wang, J., Eliora, N., Heikes, K.L., and Munjal, A. (2025). Versican controlled by Lmx1b regulates hyaluronate density and hydration for semicircular canal morphogenesis. Development *152*, dev203003. https://doi.org/10.1242/dev.203003.

12. Whitfield, T.T. (2015). Development of the inner ear. Curr. Opin. Genet. Dev. *32*, 112–118. https://doi.org/10.1016/j.gde.2015.02.006.

13. Haddon, C.M., and Lewis, J.H. (1991). Hyaluronan as a propellant for epithelial movement: the development of semicircular canals in the inner ear of Xenopus. Development *112*, 541–550. https://doi.org/10.1242/dev.112.2.541.

14. Levic, D.S., Yamaguchi, N., Wang, S., Knaut, H., and Bagnat, M. (2021). Knock-in tagging in zebrafish facilitated by insertion into non-coding regions. Development *148*. https://doi.org/10.1242/dev.199994.

15. Geng, F.-S., Abbas, L., Baxendale, S., Holdsworth, C.J., Swanson, A.G., Slanchev, K., Hammerschmidt, M., Topczewski, J., and Whitfield, T.T. (2013). Semicircular canal morphogenesis in the zebrafish inner ear requires the function of gpr126 (lauscher), an adhesion class G protein-coupled receptor gene. Development *140*, 4362–4374. https://doi.org/10.1242/dev.098061.

16. Skouloudaki, K., Puetz, M., Simons, M., Courbard, J.-R., Boehlke, C., Hartleben, B., Engel, C., Moeller, M.J., Englert, C., Bollig, F., et al. (2009). Scribble participates in Hippo signaling and is required for normal zebrafish pronephros development. Proc. Natl. Acad. Sci. U. S. A. *106*, 8579–8584. https://doi.org/10.1073/pnas.0811691106.

17. Swinburne, I. (2025). A single-cell atlas of inner ear morphogenesis in zebrafish (Biorxiv 250924). (Zenodo). https://doi.org/10.5281/ZENODO.17188954 https://doi.org/10.5281/ZENODO.17188954.

18. Swinburne, I.A., Munjal, A., Kukreja, K., Williams, S., Kawanishi, T., O'Brown, N., Ishimatsu, K., Klein, A., and Megason, S.G. (2025). A single-cell transcriptomic atlas of inner ear morphogenesis in zebrafish. bioRxiv, 2025.09.30.679639. https://doi.org/10.1101/2025.09.30.679639.

19. Farrell, J.A., Wang, Y., Riesenfeld, S.J., Shekhar, K., Regev, A., and Schier, A.F. (2018). Single-cell reconstruction of developmental trajectories during zebrafish embryogenesis. Science *360*. https://doi.org/10.1126/science.aar3131.

20. Sur, A., Wang, Y., Capar, P., Margolin, G., Prochaska, M.K., and Farrell, J.A. (2023). Single-cell analysis of shared signatures and transcriptional diversity during zebrafish development. Dev. Cell *58*, 3028-3047.e12. https://doi.org/10.1016/j.devcel.2023.11.001.

21. Fernando, C.A., Conrad, P.A., Bartels, C.F., Marques, T., To, M., Balow, S.A., Nakamura, Y., and Warman, M.L. (2010). Temporal and spatial expression of CCN genes in zebrafish. Dev. Dyn. *239*, 1755–1767. https://doi.org/10.1002/dvdy.22279.

22. Yeger, H., and Perbal, B. (2016). CCN family of proteins: critical modulators of the tumor cell microenvironment. J. Cell Commun. Signal. *10*, 229–240. https://doi.org/10.1007/s12079-016-0346-6.

841 23. Perbal, B. (2013). CCN proteins: A centralized communication network. J. Cell
842 Commun. Signal. *7*, 169–177. https://doi.org/10.1007/s12079-013-0193-7.

843 24. Zhao, B., Ye, X., Yu, J., Li, L., Li, W., Li, S., Yu, J., Lin, J.D., Wang, C.-Y., Chinnaiyan,
844 A.M., et al. (2008). TEAD mediates YAP-dependent gene induction and growth
845 control. Genes Dev. *22*, 1962–1971. https://doi.org/10.1101/gad.1664408.

846 25. Lee, S., Ahad, A., Luu, M., Moon, S., Caesar, J., Cardoso, W.V., Grant, M.B., and
847 Chaqour, B. (2019). CCN1-Yes-Associated Protein Feedback Loop Regulates
848 Physiological and Pathological Angiogenesis. Mol. Cell. Biol. *39*.
849 https://doi.org/10.1128/MCB.00107-19.

850 26. Park, M.-H., Kim, A.K., Manandhar, S., Oh, S.-Y., Jang, G.-H., Kang, L., Lee, D.-W.,
851 Hyeon, D.Y., Lee, S.-H., Lee, H.E., et al. (2019). CCN1 interlinks integrin and hippo
852 pathway to autoregulate tip cell activity. Elife *8*. https://doi.org/10.7554/eLife.46012.

853 27. Zhang, H., Pasolli, H.A., and Fuchs, E. (2011). Yes-associated protein (YAP)
854 transcriptional coactivator functions in balancing growth and differentiation in skin.
855 Proc. Natl. Acad. Sci. U. S. A. *108*, 2270–2275.
856 https://doi.org/10.1073/pnas.1019603108.

857 28. Pocaterra, A., Romani, P., and Dupont, S. (2020). YAP/TAZ functions and their
858 regulation at a glance. J. Cell Sci. *133*, jcs230425. https://doi.org/10.1242/jcs.230425.

859 29. Zanconato, F., Forcato, M., Battilana, G., Azzolin, L., Quaranta, E., Bodega, B.,
860 Rosato, A., Bicciato, S., Cordenonsi, M., and Piccolo, S. (2015). Genome-wide
861 association between YAP/TAZ/TEAD and AP-1 at enhancers drives oncogenic
862 growth. Nat. Cell Biol. *17*, 1218–1227. https://doi.org/10.1038/ncb3216.

863 30. Benhaddou, A., Keime, C., Ye, T., Morlon, A., Michel, I., Jost, B., Mengus, G., and
864 Davidson, I. (2012). Transcription factor TEAD4 regulates expression of myogenin
865 and the unfolded protein response genes during C2C12 cell differentiation. Cell
866 Death Differ. *19*, 220–231. https://doi.org/10.1038/cdd.2011.87.

867 31. Choi, H.M.T., Schwarzkopf, M., Fornace, M.E., Acharya, A., Artavanis, G., Stegmaier,
868 J., Cunha, A., and Pierce, N.A. (2018). Third-generation in situ hybridization chain
869 reaction: multiplexed, quantitative, sensitive, versatile, robust. Development *145*.
870 https://doi.org/10.1242/dev.165753.

871 32. Swinburne, I. (2025). A single-cell atlas of inner ear morphogenesis in zebrafish
872 (Biorxiv 250924). (Zenodo). https://doi.org/10.5281/ZENODO.17188953
873 https://doi.org/10.5281/ZENODO.17188953.

874 33. Kurundkar, A.R., Kurundkar, D., Rangarajan, S., Locy, M.L., Zhou, Y., Liu, R.-M.,
875 Zmijewski, J., and Thannickal, V.J. (2016). The matricellular protein CCN1 enhances
876 TGF-β1/SMAD3-dependent profibrotic signaling in fibroblasts and contributes to
877 fibrogenic responses to lung injury. FASEB J. *30*, 2135–2150.
878 https://doi.org/10.1096/fj.201500173.

879 34. Nishida, T., Kawaki, H., Baxter, R.M., Deyoung, R.A., Takigawa, M., and Lyons, K.M.
880 (2007). CCN2 (Connective Tissue Growth Factor) is essential for extracellular matrix
881 production and integrin signaling in chondrocytes. J. Cell Commun. Signal. *1*, 45–58.
882 https://doi.org/10.1007/s12079-007-0005-z.

883 35. Wong, M., Kireeva, M.L., Kolesnikova, T.V., and Lau, L.F. (1997). Cyr61, product of
884 a growth factor-inducible immediate-early gene, regulates chondrogenesis in mouse
885 limb bud mesenchymal cells. Dev. Biol. *192*, 492–508.
886 https://doi.org/10.1006/dbio.1997.8766.

887 36. Mateus, R., Lourenço, R., Fang, Y., Brito, G., Farinho, A., Valério, F., and Jacinto, A.
888 (2015). Control of tissue growth by Yap relies on cell density and F-actin in zebrafish
889 fin regeneration. Development *142*, 2752–2763. https://doi.org/10.1242/dev.119701.

890 37. Jean, R.P., Gray, D.S., Spector, A.A., and Chen, C.S. (2004). Characterization of the
891 nuclear deformation caused by changes in endothelial cell shape. J. Biomech. Eng.
892 *126*, 552–558. https://doi.org/10.1115/1.1800559.

893 38. Venturini, V., Pezzano, F., Castro, F.C., Häkkinen, H.-M., Jiménez-Delgado, S.,
894 Colomer-Rosell, M., Marro, M., Tolosa-Ramon, Q., Paz-López, S., Valverde, M.A.,
895 et al. (2020). The nucleus measures shape changes for cellular proprioception to
896 control dynamic cell behavior. Science *370*, eaba2644.
897 https://doi.org/10.1126/science.aba2644.

898 39. Torregrosa-Carrión, R., Piñeiro-Sabarís, R., Siguero-Álvarez, M., Grego-Bessa, J.,
899 Luna-Zurita, L., Fernandes, V.S., MacGrogan, D., Stainier, D.Y.R., and de la Pompa,
900 J.L. (2021). Adhesion G protein-coupled receptor Gpr126/Adgrg6 is essential for
901 placental development. Sci Adv *7*, eabj5445. https://doi.org/10.1126/sciadv.abj5445.

902 40. Bian, F., Hansen, V., Feng, H.C., He, J., Chen, Y., Feng, K., Ebrahimi, B., Gray, R.S.,
903 Chai, Y., Wu, C.-L., et al. (2024). The G protein-coupled receptor ADGRG6 maintains
904 mouse growth plate homeostasis through IHH signaling. J. Bone Miner. Res. *39*,
905 1644–1658. https://doi.org/10.1093/jbmr/zjae144.

906 41. Pogoda, H.-M., Sternheim, N., Lyons, D.A., Diamond, B., Hawkins, T.A., Woods, I.G.,
907 Bhatt, D.H., Franzini-Armstrong, C., Dominguez, C., Arana, N., et al. (2006). A
908 genetic screen identifies genes essential for development of myelinated axons in
909 zebrafish. Dev. Biol. *298*, 118–131. https://doi.org/10.1016/j.ydbio.2006.06.021.

910 42. Mogha, A., Benesh, A.E., Patra, C., Engel, F.B., Schöneberg, T., Liebscher, I., and
911 Monk, K.R. (2013). Gpr126 functions in Schwann cells to control differentiation and
912 myelination via G-protein activation. J. Neurosci. *33*, 17976–17985.
913 https://doi.org/10.1523/JNEUROSCI.1809-13.2013.

914 43. Petersen, S.C., Luo, R., Liebscher, I., Giera, S., Jeong, S.-J., Mogha, A., Ghidinelli,
915 M., Feltri, M.L., Schöneberg, T., Piao, X., et al. (2015). The adhesion GPCR GPR126
916 has distinct, domain-dependent functions in Schwann cell development mediated by

917 interaction with laminin-211. Neuron *85*, 755–769.
918 https://doi.org/10.1016/j.neuron.2014.12.057.

919 44. Seamon, K., and Daly, J.W. (1981). Activation of adenylate cyclase by the diterpene
920 forskolin does not require the guanine nucleotide regulatory protein. J. Biol. Chem.
921 *256*, 9799–9801. https://doi.org/10.1016/s0021-9258(19)68694-1.

922 45. Gonzalez, G.A., and Montminy, M.R. (1989). Cyclic AMP stimulates somatostatin
923 gene transcription by phosphorylation of CREB at serine 133. Cell *59*, 675–680.
924 https://doi.org/10.1016/0092-8674(89)90013-5.

925 46. Dobroff, A.S., Wang, H., Melnikova, V.O., Villares, G.J., Zigler, M., Huang, L., and
926 Bar-Eli, M. (2009). Silencing cAMP-response element-binding protein (CREB)
927 identifies CYR61 as a tumor suppressor gene in melanoma. J. Biol. Chem. *284*,
928 26194–26206. https://doi.org/10.1074/jbc.M109.019836.

929 47. Yu, Z., Kong, Q., and Kone, B.C. (2010). CREB trans-activation of disruptor of
930 telomeric silencing-1 mediates forskolin inhibition of CTGF transcription in mesangial
931 cells. Am. J. Physiol. Renal Physiol. *298*, F617-24.
932 https://doi.org/10.1152/ajprenal.00636.2009.

933 48. Inhibition Protein Kinase Phenocopies Ectopic Expression ofhedgehogin CNS Wild-
934 Type andcyclopsMutant Embryos.

935 49. Aragona, M., Panciera, T., Manfrin, A., Giulitti, S., Michielin, F., Elvassore, N., Dupont,
936 S., and Piccolo, S. (2013). A mechanical checkpoint controls multicellular growth
937 through YAP/TAZ regulation by actin-processing factors. Cell *154*, 1047–1059.
938 https://doi.org/10.1016/j.cell.2013.07.042.

939 50. Mason, D.E., Collins, J.M., Dawahare, J.H., Nguyen, T.D., Lin, Y., Voytik-Harbin, S.L.,
940 Zorlutuna, P., Yoder, M.C., and Boerckel, J.D. (2019). YAP and TAZ limit cytoskeletal
941 and focal adhesion maturation to enable persistent cell motility. J. Cell Biol. *218*,
942 1369–1389. https://doi.org/10.1083/jcb.201806065.

943 51. Mason, D.E., Goeckel, M., Vega, S.L., Wu, P.-H., Johnson, D., Heo, S.-J., Wirtz, D.,
944 Burdick, J.A., Wood, L., Chow, B., et al. (2023). Mechanotransductive feedback
945 control of endothelial cell motility and vascular morphogenesis.
946 https://doi.org/10.7554/elife.86668.1.

947 52. Panciera, T., Azzolin, L., Cordenonsi, M., and Piccolo, S. (2017). Mechanobiology of
948 YAP and TAZ in physiology and disease. Nat. Rev. Mol. Cell Biol. *18*, 758–770.
949 https://doi.org/10.1038/nrm.2017.87.

950 53. Lau, L.F. (2016). Cell surface receptors for CCN proteins. J. Cell Commun. Signal.
951 *10*, 121–127. https://doi.org/10.1007/s12079-016-0324-z.

952 54. Wang, X., Li, L., and Liu, D. (2014). Expression analysis of integrin β1 isoforms
953 during zebrafish embryonic development. Gene Expr. Patterns *16*, 86–92.
954 https://doi.org/10.1016/j.gep.2014.10.001.

955 55. Littlewood Evans, A., and Müller, U. (2000). Stereocilia defects in the sensory hair
956 cells of the inner ear in mice deficient in integrin alpha8beta1. Nat. Genet. *24*, 424–
957 428. https://doi.org/10.1038/74286.

958 56. Kechagia, J.Z., Ivaska, J., and Roca-Cusachs, P. (2019). Integrins as biomechanical
959 sensors of the microenvironment. Nat. Rev. Mol. Cell Biol. *20*, 457–473.
960 https://doi.org/10.1038/s41580-019-0134-2.

961 57. Monk, K.R., Oshima, K., Jörs, S., Heller, S., and Talbot, W.S. (2011). Gpr126 is
962 essential for peripheral nerve development and myelination in mammals.
963 Development *138*, 2673–2680. https://doi.org/10.1242/dev.062224.

964 58. Patra, C., van Amerongen, M.J., Ghosh, S., Ricciardi, F., Sajjad, A., Novoyatleva, T.,
965 Mogha, A., Monk, K.R., Mühlfeld, C., and Engel, F.B. (2013). Organ-specific function
966 of adhesion G protein-coupled receptor GPR126 is domain-dependent. Proc. Natl.
967 Acad. Sci. U. S. A. *110*, 16898–16903. https://doi.org/10.1073/pnas.1304837110.

968 59. Lu, S., Liu, S., Wietelmann, A., Kojonazarov, B., Atzberger, A., Tang, C., Schermuly,
969 R.T., Gröne, H.-J., and Offermanns, S. (2017). Developmental vascular remodeling
970 defects and postnatal kidney failure in mice lacking Gpr116 (Adgrf5) and Eltd1
971 (Adgrl4). PLoS One *12*, e0183166. https://doi.org/10.1371/journal.pone.0183166.

972 60. Lala, T., and Hall, R.A. (2022). Adhesion G protein-coupled receptors: structure,
973 signaling, physiology, and pathophysiology. Physiol. Rev. *102*, 1587–1624.
974 https://doi.org/10.1152/physrev.00027.2021.

975 61. Paavola, K.J., Sidik, H., Zuchero, J.B., Eckart, M., and Talbot, W.S. (2014). Type IV
976 collagen is an activating ligand for the adhesion G protein-coupled receptor GPR126.
977 Sci. Signal. *7*, ra76. https://doi.org/10.1126/scisignal.2005347.

978 62. Mitgau, J., Franke, J., Schinner, C., Stephan, G., Berndt, S., Placantonakis, D.G.,
979 Kalwa, H., Spindler, V., Wilde, C., and Liebscher, I. (2022). The N Terminus of
980 Adhesion G Protein-Coupled Receptor GPR126/ADGRG6 as Allosteric Force
981 Integrator. Front Cell Dev Biol *10*, 873278. https://doi.org/10.3389/fcell.2022.873278.

982 63. Li, Q., Huo, A., Li, M., Wang, J., Yin, Q., Chen, L., Chu, X., Qin, Y., Qi, Y., Li, Y., et
983 al. (2024). Structure, ligands, and roles of GPR126/ADGRG6 in the development and
984 diseases. Genes Dis *11*, 294–305. https://doi.org/10.1016/j.gendis.2023.02.016.

985 64. Wilde, C., Mitgau, J., Suchý, T., Schöneberg, T., and Liebscher, I. (2022). Translating
986 the force-mechano-sensing GPCRs. Am. J. Physiol. Cell Physiol. *322*, C1047–
987 C1060. https://doi.org/10.1152/ajpcell.00465.2021.

65. Behrndt, M., Salbreux, G., Campinho, P., Hauschild, R., Oswald, F., Roensch, J., Grill, S.W., and Heisenberg, C.-P. (2012). Forces driving epithelial spreading in zebrafish gastrulation. Science *338*, 257–260. https://doi.org/10.1126/science.1224143.

66. Gerety, S.S., and Wilkinson, D.G. (2011). Morpholino artifacts provide pitfalls and reveal a novel role for pro-apoptotic genes in hindbrain boundary development. Dev. Biol. *350*, 279–289. https://doi.org/10.1016/j.ydbio.2010.11.030.

67. Sorlien, E.L., Witucki, M.A., and Ogas, J. (2018). Efficient Production and Identification of CRISPR/Cas9-generated Gene Knockouts in the Model System Danio rerio. J. Vis. Exp. https://doi.org/10.3791/56969.

68. Wan, Y., Otsuna, H., Chien, C.-B., and Hansen, C. (2012). FluoRender: An application of 2D image space methods for 3D and 4D confocal microscopy data visualization in neurobiology research. IEEE Pac. Vis. Symp., 201–208. https://doi.org/10.1109/pacificvis.2012.6183592.

69. Stuart, T., Butler, A., Hoffman, P., Hafemeister, C., Papalexi, E., Mauck, W.M., III, Hao, Y., Stoeckius, M., Smibert, P., and Satija, R. (2019). Comprehensive integration of single-cell data. Cell *177*, 1888-1902.e21. https://doi.org/10.1016/j.cell.2019.05.031.

70. Blondel, V.D., Guillaume, J.-L., Lambiotte, R., and Lefebvre, E. (2008). Fast unfolding of communities in large networks. J. Stat. Mech. *2008*, P10008. https://doi.org/10.1088/1742-5468/2008/10/p10008.

71. Schultz, J., Milpetz, F., Bork, P., and Ponting, C.P. (1998). SMART, a simple modular architecture research tool: identification of signaling domains. Proc. Natl. Acad. Sci. U. S. A. *95*, 5857–5864. https://doi.org/10.1073/pnas.95.11.5857.

72. Letunic, I., Khedkar, S., and Bork, P. (2021). SMART: recent updates, new developments and status in 2020. Nucleic Acids Res. *49*, D458–D460. https://doi.org/10.1093/nar/gkaa937.

73. Sievers, F., and Higgins, D.G. (2014). Clustal Omega, accurate alignment of very large numbers of sequences. Methods Mol. Biol. *1079*, 105–116. https://doi.org/10.1007/978-1-62703-646-7_6.

74. Schindelin, J., Arganda-Carreras, I., Frise, E., Kaynig, V., Longair, M., Pietzsch, T., Preibisch, S., Rueden, C., Saalfeld, S., Schmid, B., et al. (2012). Fiji: an open-source platform for biological-image analysis. Nat. Methods *9*, 676–682. https://doi.org/10.1038/nmeth.2019.

75. De Simone, A., Evanitsky, M.N., Hayden, L., Cox, B.D., Wang, J., Tornini, V.A., Ou, J., Chao, A., Poss, K.D., and Di Talia, S. (2021). Control of osteoblast regeneration by a train of Erk activity waves. Nature *590*, 129–133. https://doi.org/10.1038/s41586-020-03085-8.

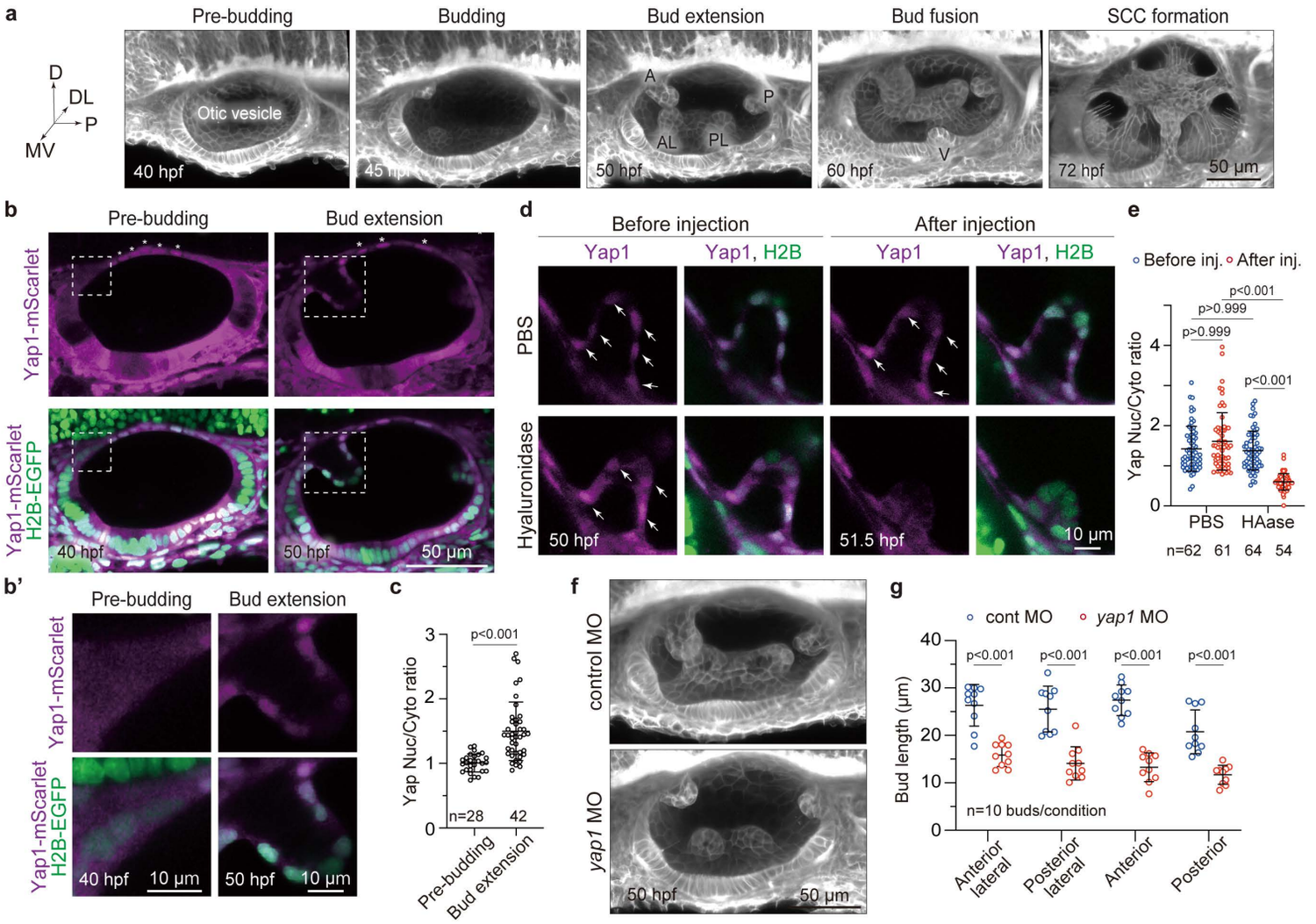
a
Pre-budding
Budding
Bud extension
Bud fusion
SCC formation
D
DL
P
MV
Otic vesicle
40 hpf
45 hpf
A
P
AL
PL
50 hpf
V
60 hpf
72 hpf
50 µm
b
Pre-budding
Bud extension
Yap1-mScarlet
Yap1-mScarlet
H2B-EGFP
40 hpf
50 hpf
50 µm
d
Before injection
After injection
Yap1
Yap1, H2B
Yap1
Yap1, H2B
PBS
Hyaluronidase
50 hpf
51.5 hpf
10 µm
e
Before inj.
After inj.
Yap Nuc/Cyto ratio
p<0.001
p>0.999
p>0.999
p<0.001
PBS
HAase
n=62 61 64 54
b'
Pre-budding
Bud extension
Yap1-mScarlet
Yap1-mScarlet
H2B-EGFP
40 hpf
10 µm
50 hpf
10 µm
c
Yap Nuc/Cyto ratio
p<0.001
n=28 42
Pre-budding
Bud extension
f
control MO
yap1 MO
50 hpf
50 µm
g
cont MO
yap1 MO
Bud length (µm)
p<0.001
p<0.001
p<0.001
p<0.001
n=10 buds/condition
Anterior lateral
Posterior lateral
Anterior
Posterior

Figure 1

Figure 1: ECM swelling-mediated Yap activation is required for bud extension

(a) Three-dimensional (3D) rendered OVs imaged at selected time points using *Tg(actb2:membrane-neongreen-neongreen)* embryos. A, anterior bud; AL, anterior-lateral bud; P, posterior bud; PL, posterior-lateral bud; V, ventral bud. Developmental stages shown in hours post fertilization (hpf). Scale bar: 50 μm.

(b-b') Two-dimensional (2D) sections of OVs imaged at selected time points using H2B-EGFP mRNA injected *TgKI(Yap1-mScarlet)* embryos. Insets (b') show enlarged images of the anterior pre-budding or budding region corresponding to the white boxes in (b). Dorsal epithelial cells with nuclear-Yap localization are indicated by asterisks. Scale bar: 10 or 50 μm. Representative images from three independent experiments are shown.

(c) Quantification of the Yap nuclear-to-cytoplasmic ratio in the cells at the anterior pre-budding or budding region at selected time points. Data are mean ± SD. *n* denotes the number of cells measured per condition from seven individual embryos from three independent experiments. *P*-value as labeled (Mann-Whitney test).

(d-e) Effect of hyaluronidase injection on Yap nuclear translocation. (d) 2D sections of the anterior bud in *TgKI(Yap1-mScarlet)*, injected with H2B-EGFP mRNA, imaged before and at 1.5 hours post-injection (hpi) of PBS or HAase. Pre-injection and post-injection images were acquired from the same individual embryos. Arrows indicate Yap1 translocated to the nucleus. Scale bar: 10 μm. Representative images from two independent experiments are shown. (e) Quantification of the Yap nuclear-to-cytoplasmic ratio in the anterior bud before and at 1.5 hpi of PBS or HAase. Data are mean ± SD. *n* denotes the number of cells measured per condition from ten individual embryos from two independent experiments. *P*-values as labeled (Kruskal–Wallis test with Dunn's test).

(f-g) Effect of *yap1* knockdown on bud growth. (f) 3D-rendered OVs from *Tg(actb2:membrane-neongreen-neongreen)* embryos, injected with control or *yap1* MO, imaged at 50 hpf. Scale bar: 50 μm. Representative images from two independent experiments are shown. (g) Quantification of bud length in embryos injected with control or *yap1* MO at 50 hpf. Data are mean ± SD. *n* denotes the number of buds from individual embryos measured per condition from two independent experiments. *P*-values as labeled (unpaired two-tailed Student's t-test).

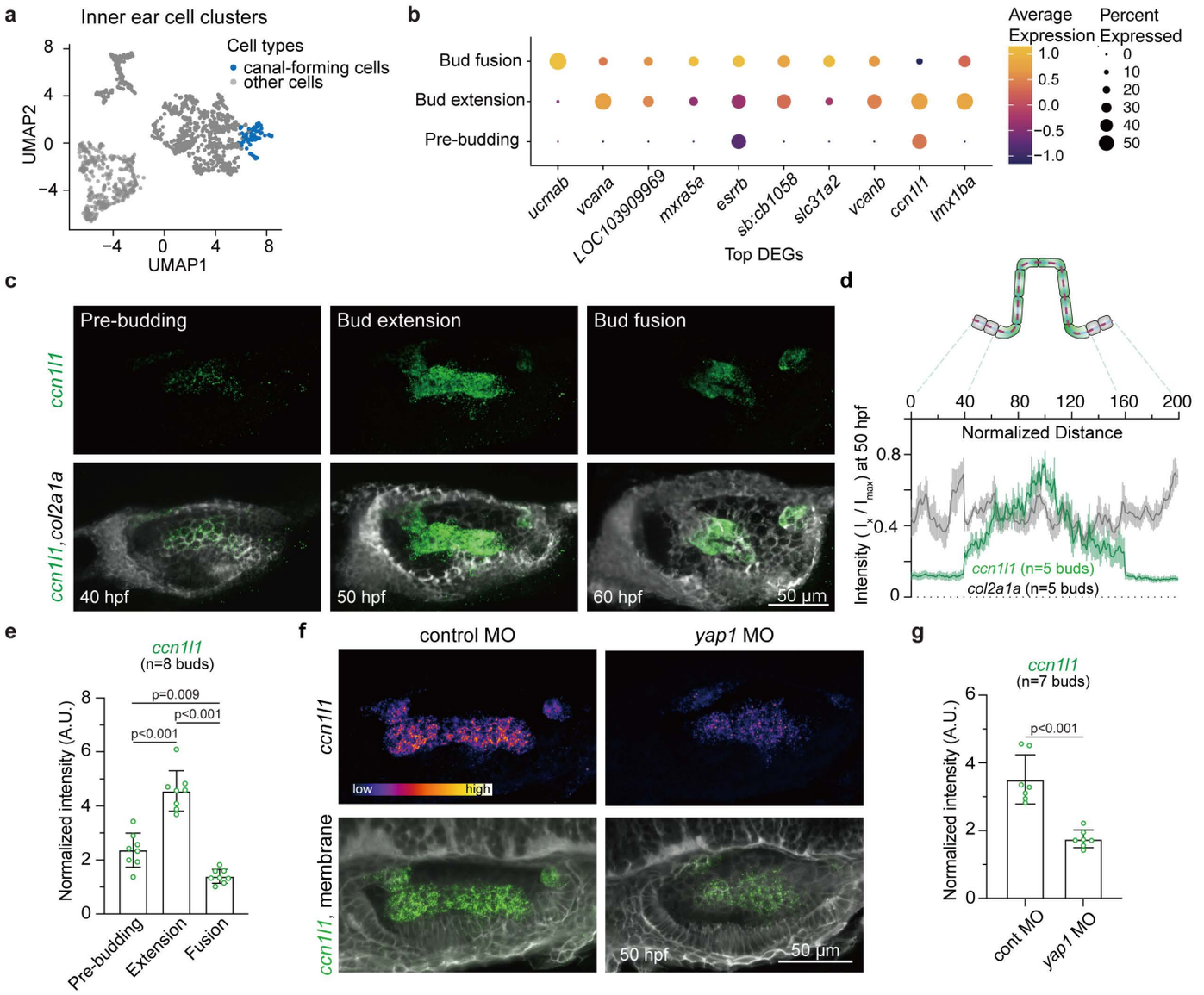
a
Inner ear cell clusters
Cell types
canal-forming cells
other cells
UMAP2
UMAP1
b
Bud fusion
Bud extension
Pre-budding
ucmab
vcana
LOC103909969
mxra5a
esrrb
sb:cb1058
slc31a2
vcanb
ccn1l1
lmx1ba
Top DEGs
Average Expression
Percent Expressed
c
Pre-budding
Bud extension
Bud fusion
ccn1l1
ccn1l1,col2a1a
40 hpf
50 hpf
60 hpf
50 µm
d
Normalized Distance
Intensity (Ix / Imax) at 50 hpf
ccn1l1 (n=5 buds)
col2a1a (n=5 buds)
e
ccn1l1
(n=8 buds)
Normalized intensity (A.U.)
p=0.009
p<0.001
p<0.001
Pre-budding
Extension
Fusion
f
control MO
yap1 MO
ccn1l1
low
high
ccn1l1, membrane
50 hpf
50 µm
g
ccn1l1
(n=7 buds)
Normalized intensity (A.U.)
p<0.001
cont MO
yap1 MO

Figure 2

Figure 2: *ccn1l1*, a Yap target gene, is enriched in the canal-genesis zone during SCC formation

(a) UMAP of single-cell RNA of the inner ear cell clusters from the DanioCell dataset. Single cells in the canal-forming cell cluster are colored blue.

(b) Dot plot showing the expression levels of the top 10 DEGs in the canal-forming cell cluster during SCC formation: pre-budding (36-40 hpf), bud extension (45-50 hpf), and bud fusion (60-72 hpf) stages. Color encodes the normalized gene expression level, and the dot size encodes the percentage of positive cells within a cluster.

(c) 3D-rendered OVs at select time points stained with multiplex *in situ* probes against *ccn1l1* (green) and *col2a1a* (white). Scale bar: 50 μm. Representative images from three independent experiments are shown.

(d) Normalized fluorescence probe intensities of *ccn1l1* or *col2a1a* genes across the illustrated region of interest (ROI) at 50 hpf indicated by the red dashed line along the anterior bud. Data are mean ± SEM. *n* denotes the number of buds from individual embryos measured per condition from three independent experiments.

(e) Comparison of normalized fluorescence probe intensity of *ccn1l1* in the anterior pre-budding, budding, or pillar region at each stage. Data are mean ± SD. *n* denotes the number of buds or pillars from individual embryos measured from two independent experiments. *P*-values as labeled (one-way ANOVA with Tukey's test).

(f-g) Effect of *yap1* knockdown on *ccn1l1* expression. (f) 3D-rendered OVs from *Tg(actb2:membrane-neongreen-neongreen)* embryos at 50 hpf stained with multiplex *in situ* probes against *ccn1l1* (green). Heatmap represents fluorescence intensity with the same contrast for the *ccn1l1* probe of embryos injected with control and *yap1* MO. Scale bar: 50 μm. Representative images from two independent experiments are shown. (g) Quantification of probe fluorescence intensity of *ccn1l1* probe in anterior buds. Data are mean ± SD. *n* denotes the number of buds from individual embryos measured from two independent experiments. *P*-value as labeled (unpaired two-tailed Student’s t-test).

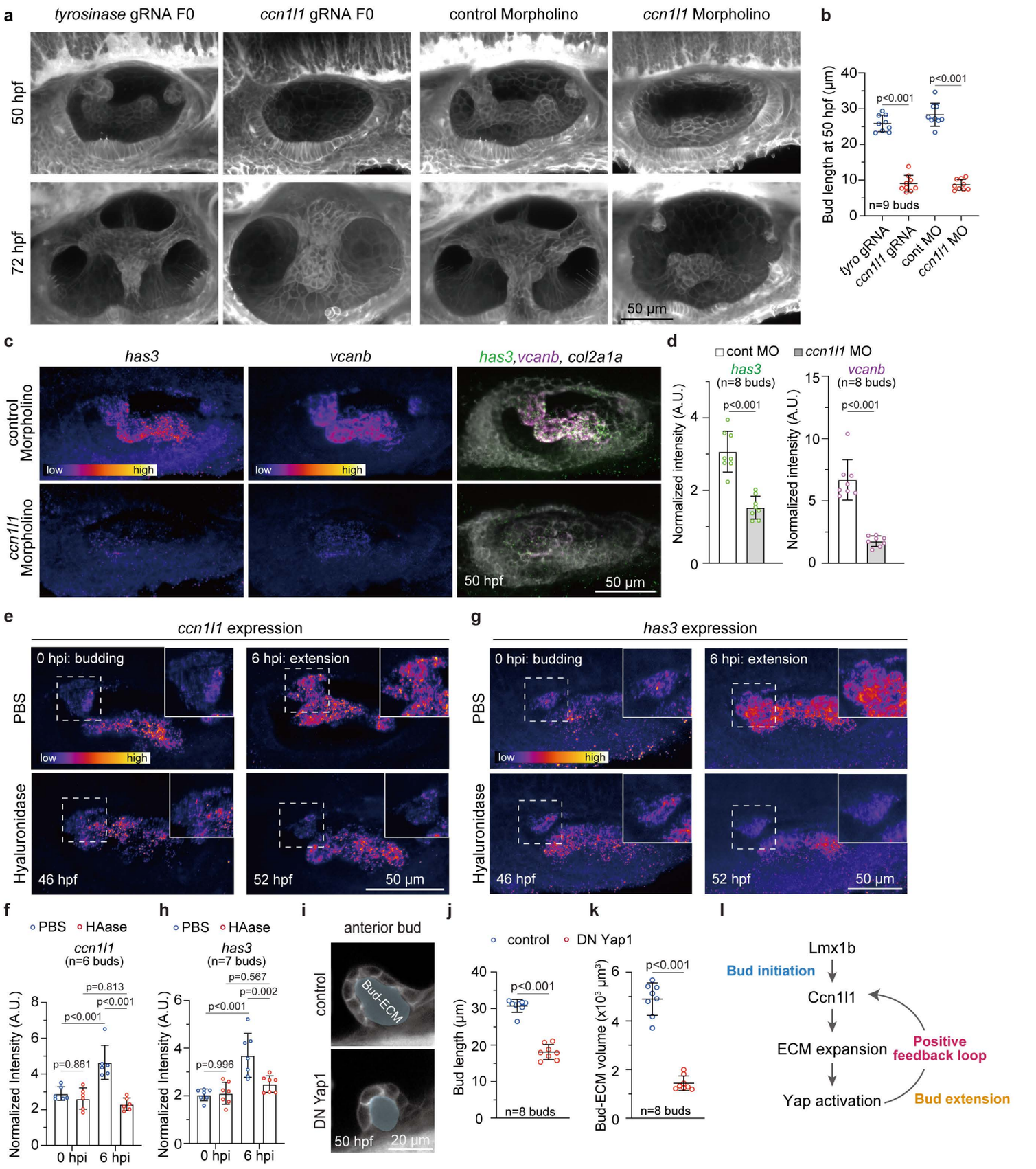
a
tyrosinase gRNA F0
ccn1l1 gRNA F0
control Morpholino
ccn1l1 Morpholino
50 hpf
72 hpf
50 µm
b
Bud length at 50 hpf (µm)
p<0.001
p<0.001
n=9 buds
tyro gRNA
ccn1l1 gRNA
cont MO
ccn1l1 MO
c
has3
vcanb
has3,vcanb, col2a1a
control Morpholino
ccn1l1 Morpholino
low
high
50 hpf
50 µm
d
cont MO
ccn1l1 MO
has3 (n=8 buds)
vcanb (n=8 buds)
Normalized intensity (A.U.)
p<0.001
p<0.001
e
ccn1l1 expression
0 hpi: budding
6 hpi: extension
PBS
Hyaluronidase
46 hpf
52 hpf
50 µm
g
has3 expression
0 hpi: budding
6 hpi: extension
PBS
Hyaluronidase
46 hpf
52 hpf
50 µm
f
PBS
HAase
ccn1l1 (n=6 buds)
Normalized Intensity (A.U.)
p=0.813
p<0.001
p<0.001
p=0.861
0 hpi
6 hpi
h
PBS
HAase
has3 (n=7 buds)
Normalized Intensity (A.U.)
p=0.567
p=0.002
p<0.001
p=0.996
0 hpi
6 hpi
i
anterior bud
control
DN Yap1
Bud-ECM
50 hpf
20 µm
j
control
DN Yap1
Bud length (µm)
p<0.001
n=8 buds
k
Bud-ECM volume (x10³ µm³)
p<0.001
n=8 buds
l
Lmx1b
Bud initiation
Ccn1l1
ECM expansion
Positive feedback loop
Yap activation
Bud extension

Figure 3

Figure 3: Ccn1l1 induces ECM production and drives the positive feedback loop via Yap mechanotransduction

(a-b) Effect of *ccn1l1* knockdown on bud growth. (a) 3D-rendered OVs from *Tg(actb2:membrane-neongreen-neongreen)* embryos, injected with *tyrosinase* gRNA, *ccn1l1* gRNA, control MO or *ccn1l1* MO, imaged at 50 hpf. Scale bar: 50 µm. Representative images from three independent experiments are shown. *tyrosinase* gRNA is used as a gRNA injection control because it causes loss of pigmentation but does not affect SCC formation. (b) Quantification of bud length in control or *ccn1l1* knockdown embryos at 50 hpf. Data are mean ± SD. In the absence of buds, bud lengths correspond to cell height. *n* denotes the number of buds from individual embryos measured per condition from three independent experiments. *P*-values as labeled (unpaired two-tailed Student's t-test).

(c-d) Effect of *ccn1l1* knockdown on *has3* and *vcanb* expression levels in buds. (c) 3D-rendered OVs at 50 hpf stained with multiplex *in situ* probes against *has3* (green), *vcanb* (magenta), and *col2a1a* (white). Heatmaps represent fluorescence intensity with the same contrast for each probe of embryos injected with control or *ccn1l1* MO. Scale bar: 50 µm. Representative images from two independent experiments are shown. (d) Quantification of probe fluorescence intensity of *has3* or *vcanb* probe in anterior buds. Data are mean ± SD. *n* denotes the number of buds from individual embryos measured per condition from two independent experiments. *P*-values as labeled (unpaired two-tailed Student's t-test).

(e-h) Effect of hyaluronidase injection on *ccn1l1* and *has3* expression levels in buds. 3D-rendered OVs and quantification of probe fluorescence intensity of *ccn1l1* (e-f) or *has3* (g-h) at 0 or 6 hpi of PBS or HAase. Heatmaps represent fluorescence intensity with the same contrast for each probe of embryos injected with PBS or HAase. Scale bar: 50 µm. Representative images from two independent experiments are shown. Data are mean ± SD. *n* denotes the number of buds from individual embryos measured per condition from two independent experiments. *P*-values as labeled (one-way ANOVA with Tukey's test).

(i-k) Effect of DN Yap1 expression on bud extension and bud-ECM volume. (i) 2D sections of anterior buds from *Tg(hsp70l: RFP-DN Yap1)* and sibling control embryos, both *Tg(actb2:membrane-neongreen-neongreen)*, imaged at 50 hpf following heat-shock induction. Regions marked in light blue indicate the bud-ECM region measured in quantifications. Scale bar: 20 µm. Representative images from two independent experiments are shown. Quantification of bud length (j) and bud-ECM volume (k) in sibling control or DN Yap1-expressing embryos at 50 hpf. Data are mean ± SD. *n* denotes the number of buds from individual embryos measured per condition from two independent experiments. *P*-values as labeled (unpaired two-tailed Student's t-test).

(I) A schematic model of the positive mechanotransduction feedback loop during bud growth.

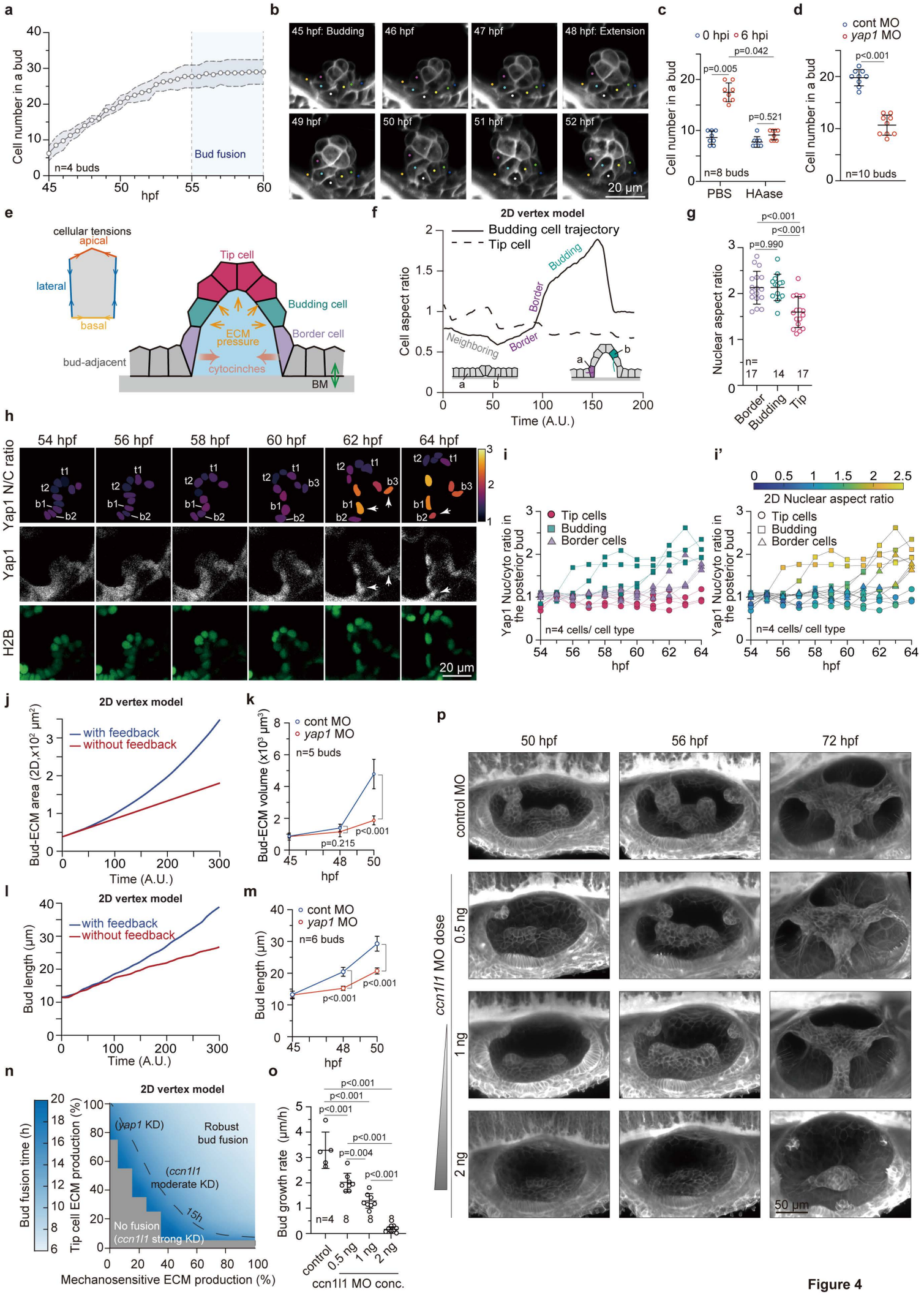
a
Cell number in a bud
hpf
n=4 buds
Bud fusion
b
45 hpf: Budding
46 hpf
47 hpf
48 hpf: Extension
49 hpf
50 hpf
51 hpf
52 hpf
20 µm
c
0 hpi
6 hpi
p=0.042
p=0.005
p=0.521
n=8 buds
PBS
HAase
d
cont MO
yap1 MO
p<0.001
n=10 buds
e
cellular tensions
apical
lateral
basal
Tip cell
Budding cell
Border cell
ECM pressure
cytocinches
bud-adjacent
BM
f
2D vertex model
Budding cell trajectory
Tip cell
Cell aspect ratio
Budding
Border
Neighboring
Time (A.U.)
g
p<0.001
p<0.001
p=0.990
Nuclear aspect ratio
n=
17
14
17
Border
Budding
Tip
h
54 hpf
56 hpf
58 hpf
60 hpf
62 hpf
64 hpf
Yap1 N/C ratio
Yap1
H2B
20 µm
i
Tip cells
Budding
Border cells
Yap1 Nuc/cyto ratio in the posterior bud
n=4 cells/ cell type
hpf
i'
2D Nuclear aspect ratio
j
2D vertex model
with feedback
without feedback
Bud-ECM area (2D,x10² µm²)
Time (A.U.)
k
cont MO
yap1 MO
n=5 buds
Bud-ECM volume (x10³ µm³)
p<0.001
p=0.215
hpf
l
2D vertex model
with feedback
without feedback
Bud length (µm)
Time (A.U.)
m
cont MO
yap1 MO
n=6 buds
Bud length (µm)
p<0.001
p<0.001
hpf
n
2D vertex model
Bud fusion time (h)
Tip cell ECM production (%)
(yap1 KD)
Robust bud fusion
(ccn1l1 moderate KD)
15h
No fusion (ccn1l1 strong KD)
Mechanosensitive ECM production (%)
o
Bud growth rate (µm/h)
p<0.001
p<0.001
p<0.001
p<0.001
p=0.004
p<0.001
n=4
8
control
0.5 ng
1 ng
2 ng
ccn1l1 MO conc.
p
50 hpf
56 hpf
72 hpf
control MO
ccn1l1 MO dose
0.5 ng
1 ng
2 ng
50 µm

Figure 4

Figure 4: Mechanical patterning by the positive feedback loop recruits adjacent cells to sustain bud extension and ensure timely fusion

(a) Quantification of cell number in the anterior bud across individual time points obtained from time-lapse imaging of *Tg(actb2:membrane-neongreen-neongreen)* embryos. Data are mean ± SD. Dashed lines indicate the range of SD at each time point. *n* denotes the number of buds from individual embryos measured from three independent experiments.

(b) 3D-rendered images of an anterior bud of the *Tg(actb2:membrane-neongreen-neongreen)* embryo at selected time points with individual cells tracked. Scale bar: 20 μm. Representative images from two independent experiments are shown.

(c) Quantification of cell number in anterior buds of embryos injected with PBS or HAase at 0 or 6 hpi. Data are mean ± SD. *n* denotes the number of buds from individual embryos measured per condition from two independent experiments. *P*-values as labeled (one-way ANOVA with Tukey's test).

(d) Quantification of cell number in anterior buds of embryos injected with control or *yap1* MO at 50 hpf. Data are mean ± SD. *n* denotes the number of buds from individual embryos measured per condition from two independent experiments. *P*-value as labeled (unpaired two-tailed Student's t-test).

(e) Schematics of the 2D vertex model simulations, showing tip, budding and border cells, as well as the relevant physical parameters. All values of physical parameters are given in the supplementary information.

(f) Trajectories of the aspect ratio of a tip cell and a recruited cell obtained with 2D vertex model simulations, exhibiting a sharp increase in aspect ratio as cell position shifts from the bud border to the budding region. Illustrations show trajectories of two individual cells from bud initiation to the end of bud extension (defined by the moment where the bud length reaches 30 μm).

(g) Quantification of 3D nuclear aspect ratio. The nuclear aspect ratio was calculated as the ratio of the long to short axes (long/short) of the ellipsoidal nucleus. Data are mean ± SD. *n* denotes the number of nuclei from individual cells measured per condition from two independent experiments. *P*-value as labeled (one-way ANOVA with Tukey's test).

(h) Time-lapse analysis of the Yap1 nuclear-to-cytoplasmic (N/C) ratio in a posterior bud of *TgKI(Yap1-mScarlet)*;*Tg(actb2:H2B-EGFP)* embryos at selected time points. Top panels show heatmaps of the Yap1 N/C ratio in individual cells of a posterior bud. Middle and bottom panels show Z-stack images of Yap1-mScarlet and H2B-EGFP, respectively. Nuclear masks used for the Yap1 N/C ratio (top panels) were generated from the H2B-EGFP signal. Yap1 N/C ratios in tip cells (t) and border cells (b) were

tracked (top panels). Cells b1, b2, and b3 show sequential Yap activation as they turn the bud border (marked by arrows). Scale bar: 20 μm. Representative images are shown from three independent experiments.

(i) Quantification of Yap N/C ratio (i) and 2D nuclear aspect ratio (i') in tip, budding, and border cells of a posterior bud across individual time points obtained from time-lapse imaging of *TgKI(Yap1-mScarlet)*; *Tg(actb2:H2B-EGFP)* embryos. The N/C ratio of individual cells was calculated every 1 hour and tracked. Heatmap in (i') represents the 2D nuclear aspect ratio in individual cells. *n* denotes the number of cells from three different posterior buds measured per condition from three independent experiments.

(j) Simulation of bud-ECM area over time, with and without mechanotransduction-driven ECM production. Tip cells are set to 100% ECM production rate.

(k) Quantification of bud-ECM volume of anterior buds in embryos injected with control or *yap1* MO at selected time points. Data are mean ± SD. *n* denotes the number of cells per condition from two independent experiments. *P*-values at selected time points as labeled (unpaired two-tailed Student's t-test).

(l) Simulation of bud length over time, with and without mechanotransduction-driven ECM production. Tip cells are set to 100% ECM production rate.

(m) Quantification of bud length of the anterior buds in embryos injected with control or *yap1* MO at selected time points. Data are mean ± SD. *n* denotes the number of cells per condition from two independent experiments. *P*-values at selected time points as labeled (unpaired two-tailed Student's t-test).

(n) Phase diagram showing the time needed for the bud to reach 30 μm and fuse, as a function of bud ECM production by budding cells (x axis) and tip cells (y axis). The region above the dotted line indicates where fusion happens in less than 15 hours after budding. Grey areas indicate regions where the bud failed to fuse (did not reach 30 μm within 22 hours after budding).

(o) Quantification of bud growth rate (μm/hour) of the anterior bud in wild-type embryos or embryos injected with *ccn1l1* MO. Data are mean ± SD. *n* denotes the number of cells per condition from one experiment. *P*-values as labeled (one-way ANOVA with Tukey's test). Growth rates for each bud were calculated over the following time ranges during bud extension stage: control (48-50 hpf); *ccn1l1* MO 0.5, 1, and 2 ng (50-56 hpf).

(p) 3D-rendered OVs from *Tg(actb2:membrane-neongreen-neongreen)* embryos, injected with control or *ccn1l1* MO, imaged at selected time points. Scale bar: 50 μm. Representative images from one experiment per condition are shown.

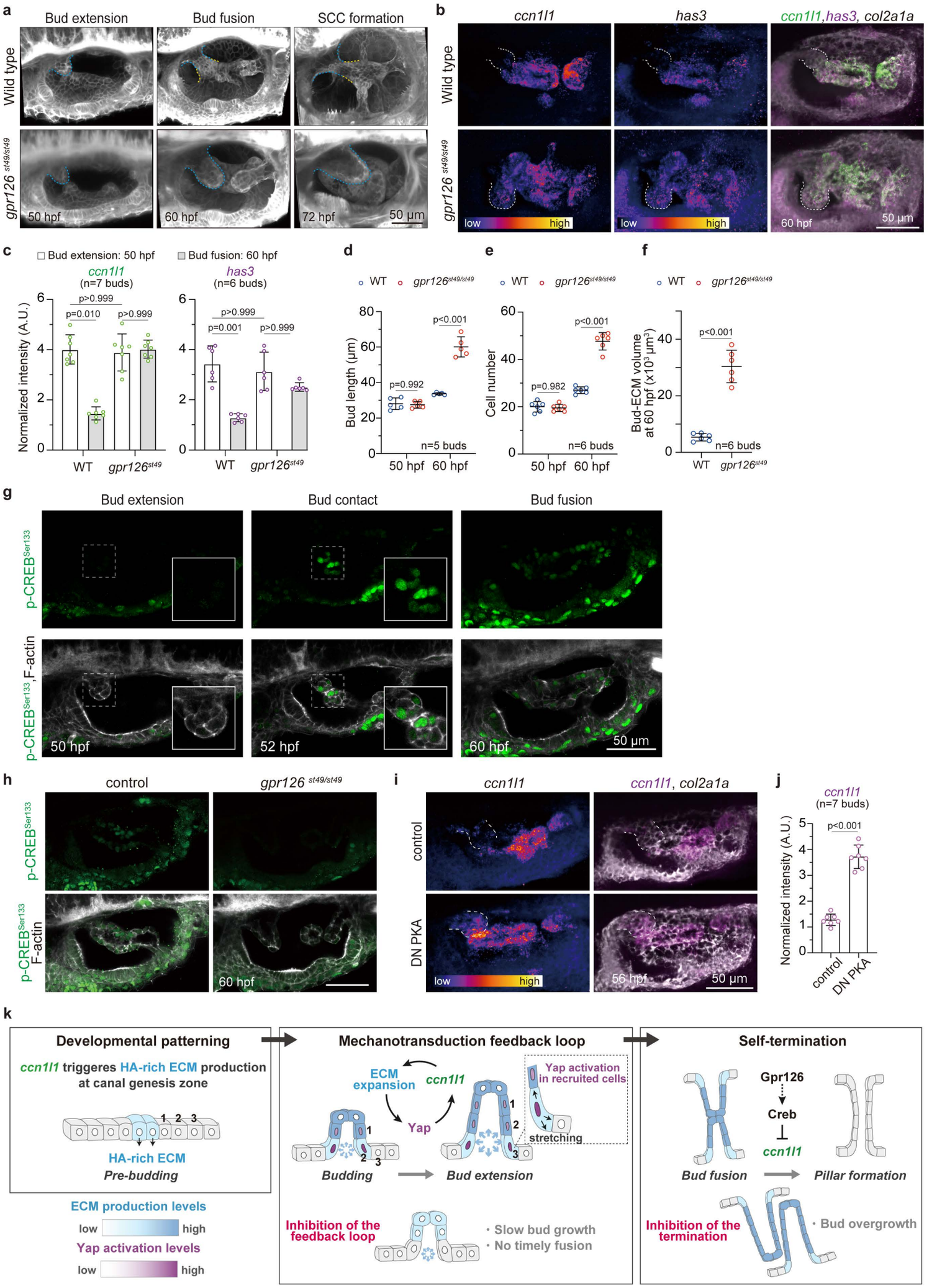
a
Bud extension
Bud fusion
SCC formation
Wild type
gpr126 st49/st49
50 hpf
60 hpf
72 hpf
50 µm
b
ccn1l1
has3
ccn1l1,has3, col2a1a
Wild type
gpr126 st49/st49
low
high
60 hpf
50 µm
c
Bud extension: 50 hpf
Bud fusion: 60 hpf
ccn1l1
(n=7 buds)
has3
(n=6 buds)
Normalized intensity (A.U.)
p>0.999
p=0.010
p>0.999
p>0.999
p=0.001
p>0.999
WT
gpr126st49
d
WT
gpr126st49/st49
Bud length (µm)
p=0.992
p<0.001
n=5 buds
50 hpf
60 hpf
e
WT
gpr126st49/st49
Cell number
p=0.982
p<0.001
n=6 buds
50 hpf
60 hpf
f
WT
gpr126st49/st49
Bud-ECM volume at 60 hpf (x10³ µm³)
p<0.001
n=6 buds
WT
gpr126st49
g
Bud extension
Bud contact
Bud fusion
p-CREBSer133
p-CREBSer133, F-actin
50 hpf
52 hpf
60 hpf
50 µm
h
control
gpr126 st49/st49
p-CREBSer133
p-CREBSer133 F-actin
60 hpf
i
ccn1l1
ccn1l1, col2a1a
control
DN PKA
low
high
56 hpf
50 µm
j
ccn1l1
(n=7 buds)
Normalized intensity (A.U.)
p<0.001
control
DN PKA
k
Developmental patterning
ccn1l1 triggers HA-rich ECM production at canal genesis zone
1 2 3
HA-rich ECM
Pre-budding
ECM production levels
low
high
Yap activation levels
low
high
Mechanotransduction feedback loop
ECM expansion
ccn1l1
Yap
Yap activation in recruited cells
stretching
Budding
Bud extension
Inhibition of the feedback loop
• Slow bud growth
• No timely fusion
Self-termination
Gpr126
Creb
ccn1l1
Bud fusion
Pillar formation
Inhibition of the termination
• Bud overgrowth

Figure 5

Figure 5: Gpr126-cAMP-PKA-CREB signaling during bud fusion suppresses *ccn1l1* expression to terminate bud extension

(a) 3D-rendered OVs from wild-type or *gpr126* $^{st49/st49}$ mutant embryos, both *Tg(actb2:membrane-neongreen-neongreen),* imaged at selected time points. Blue and yellow dashed lines indicate the anterior bud/pillar or the anterior-lateral portion of the pillar, respectively. Scale bar: 50 μm. Representative images from two independent experiments are shown.

(b-c) *ccn1l1* and *has3* expression levels in *gpr126* $^{st49/st49}$ mutant embryos. (b) 3D-rendered OVs of wild-type or *gpr126* $^{st49/st49}$ mutant embryos at 60 hpf stained with multiplex *in situ* probes against *ccn1l1* (green), *has3* (magenta), and *col2a1a* (white). Heatmaps represent fluorescence intensity with the same contrast for each probe of embryos. Scale bar: 50 μm. Representative images from three independent experiments are shown. (c) Quantification of probe fluorescence intensities of *ccn1l1* or *has3* probes in anterior buds or pillars at 50 hpf or 60 hpf. Data are mean ± SD. *n* denotes the number of buds or pillars from individual embryos measured from three independent experiments. *P*-values as labeled (Kruskal-Wallis test with Dunn's test).

(d-f) Effect of *gpr126* $^{st49/st49}$ mutation on bud growth. Quantification of bud length (d), cell number in the anterior bud or pillar (e), and bud-ECM volume (f) at selected time points. Data are mean ± SD. *n* denotes the number of buds or pillars from individual embryos measured from two independent experiments. *P*-values as labeled (unpaired two-tailed Student's t-test).

(g) 2D sections of OVs showing phospho-CREB and F-actin, stained using anti-phospho-CREB^{ser133} antibody and phalloidin, respectively, at selected time points. Insets show enlarged images of the anterior buds corresponding to the dashed white boxes. Scale bar: 50 μm. Representative images from three independent experiments are shown.

(h) 2D sections of OVs showing phospho-CREB and F-actin, stained using anti-phospho-CREB^{ser133} antibody and phalloidin, respectively, at 60 hpf in sibling control or *gpr126* $^{st49/st49}$ mutant embryos. Scale bar: 50 μm. Representative images from two independent experiments are shown.

(i-j) Effect of DN PKA on *ccn1l1* expression in buds. (i) 3D-rendered OVs from *Tg(hsp70l:DN PKA-GFP)* embryos and sibling controls after heat-shock induction, stained with multiplex *in situ* probes against *ccn1l1* (magenta) and *col2a1a* (white). Heatmaps represent fluorescence intensity with the same contrast for each *ccn1l1* probe. Scale bar: 50 μm. Representative images from three independent experiments are shown. (j) Quantification of probe fluorescence intensity of *ccn1l1* in anterior buds or pillars at 56 hpf. Data are mean ± SD. *n* denotes the number of buds or pillars from

individual embryos measured from three independent experiments. *P*-value as labeled (unpaired two-tailed Student's t-test).

(k) A schematic model of the Yap mechanotransduction feedback loop and its termination mechanism during semicircular canal formation. HA synthesis is initiated in a small group of cells during the pre-budding stage. As the ECM swells, mechanical stress at the bud border triggers Yap activation, initiating the Yap–*ccn1l1*–ECM positive feedback loop. This loop amplifies the domain by recruiting adjacent cells into the bud, sustaining rapid bud extension and ensuring timely fusion. Disrupting any component of the loop blocks extension. During fusion, Gpr126-PKA-Creb signaling is activated to terminate the feedback loop. Loss of this termination mechanism results in continued ECM production and bud overgrowth.